

1 **Global methane budget and trend, 2010-2017: complementarity of inverse analyses**
2 **using in situ (GLOBALVIEWplus CH₄ ObsPack) and satellite (GOSAT) observations**

3
4 Xiao Lu¹, Daniel J. Jacob¹, Yuzhong Zhang^{1,2,3}, Joannes D. Maasakkers⁴, Melissa P. Sulprizio¹, Lu Shen¹,
5 Zhen Qu¹, Tia R. Scarpelli¹, Hannah Nesser¹, Robert M. Yantosca¹, Jianxiong Sheng⁵, Arlyn Andrews⁶,
6 Robert J. Parker^{7,8}, Hartmut Boesch^{7,8}, A. Anthony Bloom⁹, Shuang Ma⁹

7
8 ¹Harvard John A. Paulson School of Engineering and Applied Sciences, Harvard University, Cambridge,
9 MA, USA

10 ²School of Engineering, Westlake University, Hangzhou, Zhejiang Province, China

11 ³Institute of Advanced Technology, Westlake Institute for Advanced Study, Hangzhou, Zhejiang Province,
12 China

13 ⁴SRON Netherlands Institute for Space Research, Utrecht, The Netherlands.

14 ⁵Center for Global Change Science, Massachusetts Institute of Technology, Cambridge, MA, USA

15 ⁶National Oceanic and Atmospheric Administration, Earth System Research Laboratory, Boulder, CO,
16 USA

17 ⁷National Centre for Earth Observation, University of Leicester, UK

18 ⁸Earth Observation Science, Department of Physics and Astronomy, University of Leicester, UK

19 ⁹Jet Propulsion Laboratory, California Institute of Technology, Pasadena, CA, USA

20
21 *Correspondence to:* Xiao Lu (xiaolu@g.harvard.edu) and Yuzhong Zhang
22 (zhangyuzhong@westlake.edu.cn)

24 **Abstract**

25 We use satellite (GOSAT) and in situ (GLOBALVIEWplus CH4 ObsPack) observations of atmospheric
26 methane in a joint global inversion of methane sources, sinks, and trends for the 2010-2017 period. The
27 inversion is done by analytical solution to the Bayesian optimization problem, yielding closed-form
28 estimates of information content to assess the consistency and complementarity (or redundancy) of the
29 satellite and in situ datasets. We find that GOSAT and in situ observations are to a large extent
30 complementary, with GOSAT providing a stronger overall constraint on the global methane distributions,
31 but in situ observations being more important for northern mid-latitudes and for relaxing global error
32 correlations between methane emissions and the main methane sink (oxidation by OH radicals). The in-
33 situ-only and the GOSAT-only inversion alone, achieve respectively 113 and 212 independent pieces of
34 information (DOFS) for quantifying mean 2010-2017 anthropogenic emissions on 1009 global model
35 grid elements, and DOFS of 67 and 122 for 2010-2017 emission trends. The joint GOSAT + in situ
36 inversion achieves DOFS of 262 and 161 respectively for mean emissions and trends. The in situ data
37 thus increase the global information content from the GOSAT-only inversion by 20-30%. The in-situ-only
38 and GOSAT-only inversions show consistent corrections to regional methane emissions but are less
39 consistent in optimizing the global methane budget. The joint inversion finds that oil/gas emissions in the
40 US and Canada are underestimated relative to the values reported by these countries to the United Nations
41 Framework Convention on Climate Change (UNFCCC) and used here as prior estimates, while coal
42 emissions in China are overestimated. Wetland emissions in North America are much lower than in the
43 mean WetCHARTs inventory used as prior estimate. Oil/gas emissions in the US increase over the 2010-
44 2017 period but decrease in Canada and Europe. The joint inversion yields a global methane emission of
45 551 Tg a⁻¹ averaged over 2010-2017 and a methane lifetime of 11.2 years against oxidation by
46 tropospheric OH (86% of the methane sink).

47

48 **1 Introduction**

49 Methane (CH₄) is the second most important anthropogenic greenhouse gas, and plays a central role in
50 atmospheric chemistry as a precursor of tropospheric ozone and a sink of hydroxyl radicals (OH). It is
51 emitted from many natural and anthropogenic sources that are difficult to quantify (Saunois et al., 2020).
52 Atmospheric methane observations from satellites and in situ (surface, tower, shipboard, and aircraft)
53 platforms have been used extensively to infer methane emissions and their trends through inverse analyses
54 (Houweling et al., 2017). But the information from satellite and in situ observations does not always agree
55 (Monteil et al., 2013; Bruhwiler et al., 2017) and is hard to compare because of large differences in
56 observational density, precision, and the actual quantity being measured (Cressot et al., 2014). Here we
57 use an analytical solution to the Bayesian inverse problem to quantitatively compare and combine the
58 information from satellite (GOSAT) and in situ (GLOBALVIEWplus CH₄ ObsPack) observations for
59 estimating global methane sources and their trends over the 2010-2017 period, including contributions
60 from different source sectors and from the methane sink (oxidation by tropospheric OH).

61
62 Inverse analyses of atmospheric methane observations using chemical transport models (CTM) provide a
63 formal method for inferring methane emissions and their trends (Brasseur and Jacob, 2017). Global
64 satellite observations of atmospheric methane columns from the shortwave infrared SCIAMACHY and
65 GOSAT instruments have been widely used for this purpose (Bergamaschi et al., 2013; Wecht et al., 2014;
66 Turner et al., 2015; Maasakkers et al., 2019; Miller et al., 2019; Lunt et al., 2019). Other inverse analyses
67 have relied on in situ methane observations that have much higher precision, are more sensitive to surface
68 emissions, and may include isotopic information, but are much sparser (Pison et al, 2009; Bousquet et al.,
69 2011; Miller et al., 2013; Patra et al., 2016; McNorton et al., 2018).

70
71 A number of inverse analyses have combined in situ and satellite observations (Bergamaschi et al., 2007,
72 2009, 2013; Fraser et al., 2013; Monteil et al, 2013; Cressot et al., 2014; Houweling et al., 2014; Alexe et
73 al., 2015; Ganesan et al., 2017; Janardanan et al., 2020), but few of them have compared the information
74 from the two data streams and then mostly qualitatively. Bergamaschi et al. (2009, 2013), Fraser et al.
75 (2014), and Alexe et al. (2015) found that surface and satellite methane observations provided consistent
76 constraints on global methane emissions, but that satellite observations achieved stronger regional
77 constraints in the tropics. No study to our knowledge has compared the ability of satellite and in situ
78 observations to attribute long-term methane trends.

79
80 Analytical solution to the inverse problem, as used here, provides closed-form error characterization as
81 part of the solution, and from there allows derivation of the information content from different
82 components of the observing system (Rodgers, 2000). Application to satellite observations has been used
83 to determine where the observations can actually constrain the inverse solution (Turner et al., 2015). The
84 major obstacle to this analytical solution in the past has been the need to construct the Jacobian matrix
85 for the CTM forward model, but this is now readily done using massively parallel computing clusters
86 (Maasakkers et al., 2019). Such a method provides a means to quantify the differences in information

87 content between different data streams (e.g., satellite vs. in situ) and from there to contribute to the design
88 of a better observing system.

89

90 Here we apply satellite observations of atmospheric methane columns from the GOSAT instrument
91 together with an extensive global compilation of in situ observations (including surface, tower, shipboard,
92 and aircraft methane measurements) from the GLOBALVIEWplus CH₄ ObsPack v1.0 data product
93 (Cooperative Global Atmospheric Data Integration Project, 2019), to quantify the global distribution of
94 methane emissions, loss from reaction with OH, and related trends for the 2010-2017 period. We use for
95 this purpose an analytical inversion method that formally characterizes the information content from the
96 two data streams, whether that information is consistent, and whether it is complementary or redundant
97 (Rodgers, 2000; Jacob et al., 2016). Our work provides a comprehensive global perspective on the sources
98 contributing to 2010-2017 methane emissions and trends, as well as a general framework for synthesizing
99 the information from satellite and in situ observations.

100

101 **2 Methods**

102 Figure 1 summarizes the components of our analytical inversion system, which builds on previous
103 inversions of GOSAT satellite data by Maasakkers et al. (2019) and Zhang et al. (2020a) but adds the in
104 situ observations. We apply observations y from GLOBALVIEWplus observations and/or GOSAT
105 (Section 2.1), with the GEOS-Chem CTM as forward model (Section 2.3), to optimize the state vector x
106 of our inverse problem. The state vector has dimension $n = 3378$ including mean 2010-2017 non-wetland
107 methane emissions on the GEOS-Chem $4^\circ \times 5^\circ$ global grid ($n_1 = 1009$), 2010-2017 linear trends for these
108 emissions on that grid ($n_2 = 1009$), monthly mean wetland methane emissions for individual years in 14
109 subcontinental regions ($n_3 = 12 \times 8 \times 14 = 1344$), and tropospheric OH concentrations in each hemisphere
110 for individual years ($n_4 = 2 \times 8 = 16$). Section 2.2 describes the prior state vector estimates (x_A) and the
111 prior error covariance matrix (S_A). We derive posterior estimates \hat{x} of the state vector and the associated
112 error covariance matrix \hat{S} by analytical solution to the Bayesian optimization problem (Section 2.4). We
113 present results from three inversions using in situ observations only (in-situ-only inversion), GOSAT
114 observations only (GOSAT-only inversion), and both GOSAT and in situ observations (GOSAT + in situ
115 inversion).

116

117 **2.1 Methane observations**

118 The GLOBALVIEWplus CH₄ ObsPack v1.0 data product compiled by the National Oceanic and
119 Atmospheric Administration (NOAA) Global Monitoring Laboratory includes worldwide high-accuracy
120 measurements of atmospheric methane concentrations from different observational platforms (surface,
121 tower, shipboard, and aircraft) (Cooperative Global Atmospheric Data Integration Project, 2019). Here
122 we use the ensemble of GLOBALVIEWplus observations for 2010-2017. For surface and tower
123 measurements, we use only daytime (10-16 local time) observations and average them to the
124 corresponding daytime mean values. We exclude outliers at individual sites that depart by more than three
125 standard deviations from the mean. We obtain in this manner 157054 observation data points for the

126 inversion including 81119 from 103 surface sites, 27433 from 13 towers, 827 from 3 ship cruises, and
127 47675 from 29 aircraft campaigns. Figure 2a shows the mean methane concentrations in 2010-2017 from
128 the in situ data. The data are relatively dense in North America and western Europe, with also a few sites
129 in China, but otherwise mainly measure background concentrations. The number of available surface and
130 tower observations increases from 10493 in 2010 to 19657 in 2017 with the largest changes in Europe
131 and Canada.

132
133 GOSAT is a nadir-viewing satellite instrument launched in 2009 that measures the backscattered solar
134 radiation from a sun-synchronous orbit at around 13:00 local time (Butz et al., 2011; Kuze et al, 2016).
135 Observing pixels are 10-km in diameter and separated by about 250 km along-track and cross-track in
136 normal observation mode, with higher-density data collected in targeted observation modes. Methane is
137 retrieved at the 1.65 μm absorption band. We use dry column methane mixing ratios from the University
138 of Leicester version 9.0 Proxy XCH₄ retrieval (Parker et al., 2020). The retrieval has a single-observation
139 precision of 13 ppb and a regional bias of 2 ppb (Buchwitz et al., 2015). We use GOSAT data for 2010-
140 2017 including 1.6 million retrievals over land as shown in Figure 2b. We do not use glint data over the
141 oceans and data poleward of 60° because of seasonal bias and the potential for large errors (Maasakkers
142 et al., 2019).

143 144 **2.2 Prior estimates**

145 Table 1 summarizes the prior estimates of the mean 2010-2017 methane emissions used for the state vector,
146 and Figure 3 shows the spatial patterns. Natural sources include the ensemble mean of the WetCHARTs
147 inventory version 1.2.1 (Bloom et al., 2017) for wetlands, open fires from the Global Fire Emissions
148 Database version 4s with seasonal and interannual variability (van der Werf et al., 2017), termites from
149 Fung et al. (1991), and seeps from Etiope et al. (2019) with global scaling to 2 Tg a⁻¹ from Hmiel et al.
150 (2020). The default anthropogenic emissions are from EDGAR v4.3.2 (Janssens-Maenhout et al., 2019),
151 and are superseded for fugitive fuel emissions (oil, gas, coal) by the Scarpelli et al. (2020) inventory
152 which spatially allocates national emissions reported by countries to the United Nations Framework
153 Convention of Climate Change (UNFCCC). US anthropogenic emissions are further superseded by the
154 gridded version of Inventory of U.S. Greenhouse Gas Emissions and Sinks from the Environmental
155 Protection Agency (EPA GHGI) (Maasakkers et al., 2016). The WetCHARTs wetlands inventory includes
156 seasonal and interannual variability that is optimized in the inversion through correction to the monthly
157 emissions. Seasonality from Zhang et al. (2016) is imposed for rice emissions, and temperature-dependent
158 seasonality is applied to manure emissions (Maasakkers et al., 2016). Other emissions are aseasonal.

159
160 We assume a 50% error standard deviation for all anthropogenic and non-wetland natural emissions on
161 the 4° latitude \times 5° longitude grid, with no spatial error covariance so that their prior error covariance
162 matrix is diagonal, which is a reasonable assumption for anthropogenic emissions (Maasakkers et al.,
163 2016). We assume $0 \pm 10\%$ a⁻¹ as prior estimate for the linear 2010-2017 emission trends on the 4° \times 5°
164 grid; a sensitivity test using $0 \pm 5\%$ a⁻¹ is also performed. The inclusion of linear trends in state vectors

165 allows us to identify the direction of emission change for each $4^\circ \times 5^\circ$ grid in the 8-year period, but it
166 would not capture high-frequency interannual variability. Prior estimates of monthly mean wetland
167 methane emissions for individual years in 14 subcontinental regions, along with their error covariance
168 matrix, are from the WetCHARTs v1.2.1 inventory ensemble (Bloom et al., 2017). The prior methane
169 emissions total 533 Tg a^{-1} , at the low end of the current top-down estimates ($550\text{-}594 \text{ Tg a}^{-1}$) for 2008-
170 2017 (Saunois et al., 2020), and this largely reflects the downward revision of global seep emissions by
171 Hmiel et al. (2020).

172
173 Prior monthly 3-D fields of global tropospheric OH concentrations are taken from a GEOS-Chem
174 simulation with full chemistry (Wecht et al., 2014) that yields a methane lifetime $\tau_{\text{CH}_4}^{\text{OH}}$ due to oxidation
175 by tropospheric OH of 10.6 years and an inter-hemispheric OH ratio (North to South) of 1.16. The
176 methane lifetime is consistent with the value of 11.2 ± 1.3 years inferred from methylchloroform
177 observations (Prather et al., 2012), while the inter-hemispheric OH ratio lies between the observed range
178 of 0.97 ± 0.12 (Patra et al., 2014) and the recent multi-model estimates of 1.3 ± 0.1 (Zhao et al., 2019). We
179 assume no interannual variability in this prior OH field. We assume 10% as prior error standard deviation
180 for the hemispheric OH concentrations in individual years, based on Holmes et al. (2013), and also
181 conduct a sensitivity test assuming 5%. Corrections to OH in the inversion are applied as a hemispheric
182 scaling factor for individual years, without changing the spatial or temporal pattern of the original fields.
183 Zhang et al. (2018) conducted methane inversions with twelve different OH fields from the ACCMIP
184 model ensemble (Naik et al., 2013) and found no significant difference in results with the GEOS-Chem
185 OH fields used here except for two outlier models.

186

187 **2.3 Forward Model**

188 We use the GEOS-Chem 12.5.0 (<http://geos-chem.org>) global CTM (Bey et al., 2001; Wecht et al., 2014;
189 Maasakkers et al., 2019) as forward model to simulate atmospheric methane concentrations and their
190 sensitivity to the state vector elements. The model is driven by MERRA-2 reanalysis meteorological fields
191 from the NASA Global Modeling and Assimilation Office (GMAO) (Gelaro et al., 2017). The methane
192 sink is computed within the model from 3-D tropospheric oxidant fields including OH (optimized in the
193 inversion), Cl atoms (Wang et al., 2019), 2-D stratospheric oxidant fields (Murray et al., 2012), and soil
194 uptake (Murguia-Flores et al., 2018). We conduct GEOS-Chem model simulations for 2010-2017 at
195 global $4^\circ \times 5^\circ$ resolution with 47 vertical layers extending to the mesosphere.

196

197 GEOS-Chem has excessive methane in the high-latitudes stratosphere, a flaw common to many models
198 (Patra et al., 2011) especially at coarse model resolution. Following Zhang et al. (2020), we compute
199 correction factors to GEOS-Chem stratospheric methane subcolumns as a function of season and
200 equivalent latitude to match the measurements from the solar occultation ACE-FTS v3.6 instrument
201 (Waymark et al., 2014; Koo et al., 2017). As shown in Zhang et al. (2020), the correction can be up to 10%
202 at high latitudes during winter and spring. We apply the correction factors before the inversion to avoid
203 wrongly attributing this model transport bias to methane emissions and loss. Figure S1 shows that the

204 systematic differences in the posterior scaling factors of non-wetland emissions with vs. without bias
205 correction are more prominent at the northern high latitudes, as also shown in Stanevich et al. (2020), but
206 the global total emissions only differ by 1%.

207
208 Initial GEOS-Chem methane concentrations on January 1, 2010 are adjusted to have unbiased zonal
209 mean relative to GOSAT observations for January 2010, and we find that the resulting model values are
210 also unbiased relative to the GLOBALVIEWplus in situ observations in January 2010. In this manner,
211 model discrepancies with observations over the 2010-2017 period can be attributed to model errors in
212 emissions or OH over that period, instead of error in initial conditions. We archive model methane dry
213 mixing ratios at each location and time of the in situ and GOSAT datasets for 2010-2017.

214
215 As forward model F for the inversion, GEOS-Chem relates the state vector \mathbf{x} to the atmospheric
216 concentrations \mathbf{y} as $\mathbf{y} = F(\mathbf{x})$ (Fig.1). The simulation of observations with the prior estimates of state
217 vectors (\mathbf{x}_A) in 2010-2017 diagnoses systematic errors in comparison to observations that enable
218 improved estimate of the state vector through the inversion. In addition, the random component of the
219 discrepancy can be used to estimate the observation error (sum of instrument error, representation error,
220 and forward model error) in the Bayesian optimization problem using the residual error method (Heald et
221 al., 2004). The method assumes that the systematic component of the model bias ($\overline{\mathbf{y} - F(\mathbf{x}_A)}$) for
222 individual years, where the overbar denotes the temporal average in a $4^\circ \times 5^\circ$ grid cell (for GOSAT) or for
223 an observation platform (for in situ observations), is to be corrected in the inversion, while the residual
224 term ($\epsilon_0 = \mathbf{y} - F(\mathbf{x}_A) - \overline{\mathbf{y} - F(\mathbf{x}_A)}$) represents the random observation error. Here we applied this
225 method to construct the observation error covariance matrix \mathbf{S}_0 from the statistics of ϵ_0 . For in-situ
226 observations, we derive ϵ_0 separately for the ensemble of background surface sites (Dlugokencky et al.,
227 1994), non-background sites, tower sites, shipboard measurements, and aircraft measurements, while for
228 GOSAT observations ϵ_0 is calculated for each $4^\circ \times 5^\circ$ grid cell.

229
230 We find that the mean standard deviation of the random observation error (ϵ_0) for the GLOBALVIEWplus
231 in situ data averages 36 ppbv (20 and 45 ppbv for background and non-background surface observations,
232 68 ppbv for tower observations, 10 ppbv for shipboard observations, 24 ppbv for aircraft observations),
233 compared to 13 ppbv for GOSAT. The observation error for in situ observations is dominated by the
234 forward model error while for GOSAT it is dominated by the instrument error. The forward model error
235 is higher for surface concentrations near source regions than for columns or other in situ observations
236 measuring background, because the amplitude of methane variability is much higher (Cusworth et al.,
237 2018) and more challenging for a model at $4^\circ \times 5^\circ$ resolution to capture. We assume that \mathbf{S}_0 is diagonal
238 in the absence of better objective information, but in fact some error correlation between different
239 observations could be expected to arise from transport and source aggregation errors in the forward model.
240 This is considered by introducing a regularization factor γ in the minimization of the cost function for
241 the inversion (Section 2.4).

2.4 Analytical Inversion

The Bayesian solution to the state vector optimization problem assuming Gaussian prior and observation errors involves minimizing the cost function $J(\mathbf{x})$:

$$J(\mathbf{x}) = (\mathbf{x} - \mathbf{x}_A)^T \mathbf{S}_A^{-1} (\mathbf{x} - \mathbf{x}_A) + \gamma (\mathbf{y} - \mathbf{F}(\mathbf{x}))^T \mathbf{S}_O^{-1} (\mathbf{y} - \mathbf{F}(\mathbf{x})) \quad (1),$$

where \mathbf{x} is the state vector, \mathbf{x}_A denotes the prior estimate of \mathbf{x} , \mathbf{S}_A is the prior error covariance matrix, \mathbf{y} is the observation vector, $\mathbf{F}(\mathbf{x})$ represents the GEOS-Chem simulation of \mathbf{y} , \mathbf{S}_O is the observation error covariance matrix, and γ is a regularization factor. The need for γ in $J(\mathbf{x})$ is to avoid giving excessive weighting to observations, due to the likely underestimation of \mathbf{S}_O when unknown error correlations are not included in its construction (Zhang et al., 2018; Maasakkers et al., 2019). γ here plays the same role as the regularization parameter in Tikhonov methods (Brasseur and Jacob, 2017) and reflects our inability to properly quantify the magnitude of errors.

Minimization of the cost function in equation (1) has an analytical solution if the forward model is linear (Rodgers, 2000). The optimization of methane emission and its trends is strictly linear by design because we use prescribed monthly 3-D OH fields as described in Section 2.2. There is some non-linearity regarding the optimization of OH, because the sensitivity of the methane concentration to changes in OH concentrations depends on the methane concentration through first-order loss, but we assume that the variability of methane concentration is sufficiently small that this non-linearity is negligible (we verify this assumption below). We thus express the GEOS-Chem forward model as $\mathbf{y} = \mathbf{K}\mathbf{x} + \mathbf{c}$, where $\mathbf{K} = \partial\mathbf{y}/\partial\mathbf{x}$ represents the Jacobian matrix and \mathbf{c} is an initialization constant. We construct the Jacobian matrix \mathbf{K} explicitly by conducting GEOS-Chem simulations with each element of the state vector perturbed separately. For the linear emission trend elements, this is done by perturbing the 2010-2017 emission trend in each grid cell from 0% (the best prior estimate) to 10% a⁻¹; for OH, this is done by perturbing yearly hemispheric OH fields by 20% without modifying the spatial or seasonal distribution. Comparison of the resulting Jacobian matrix to GEOS-Chem as $\mathbf{F}(\mathbf{x}) - \mathbf{K}\mathbf{x} - \mathbf{c}$ shows a negligible residual difference of 2±3 ppb, verifying the assumption of linearity.

Minimizing the Bayesian cost function by solving $dJ(\mathbf{x})/d\mathbf{x} = \mathbf{0}$ yields closed-form expressions for the posterior estimate of the state vector $\hat{\mathbf{x}}$ with error covariance matrix $\hat{\mathbf{S}}$:

$$\hat{\mathbf{x}} = \mathbf{x}_A + \mathbf{G}(\mathbf{y} - \mathbf{K}\mathbf{x}_A) \quad (2),$$

$$\hat{\mathbf{S}} = (\gamma\mathbf{K}^T\mathbf{S}_O^{-1}\mathbf{K} + \mathbf{S}_A^{-1})^{-1} \quad (3),$$

where \mathbf{G} is the gain matrix,

$$\mathbf{G} = \frac{\partial\hat{\mathbf{x}}}{\partial\mathbf{y}} = (\gamma\mathbf{K}^T\mathbf{S}_O^{-1}\mathbf{K} + \mathbf{S}_A^{-1})^{-1}\gamma\mathbf{K}^T\mathbf{S}_O^{-1} \quad (4).$$

From the posterior error covariance matrix one can derive the averaging kernel matrix describing the sensitivity of the posterior estimate to the true state:

281
282
283
284
285
286
287
288
289
290
291
292
293
294
295
296
297
298
299
300
301
302
303
304
305
306
307
308
309
310
311
312
313
314
315
316

$$\mathbf{A} = \frac{\partial \hat{\mathbf{x}}}{\partial \mathbf{x}} = \mathbf{I}_n - \widehat{\mathbf{S}}\mathbf{S}_A^{-1} \quad (5).$$

The trace of \mathbf{A} quantifies the degrees of freedom for signal (DOFS), which represents the number of pieces of independent information gained from the observing system for constraining the state vector (Rodgers, 2000).

We choose the value of the regularization parameter γ in order to avoid overfitting to the observations when the number m of observations is much larger than the number n of state vector elements, and the error covariance of the observations cannot be properly quantified. Overfitting would be implied by a highly unlikely departure of the posterior solution from the prior estimate, which can be indicated from the posterior cost function. For a given state vector element i , the expected value of $(x_i - x_{Ai})^2$ is the prior error variance σ_{Ai}^2 . For an n -dimensional state vector with a diagonal prior error covariance matrix, the state component J_A of the cost function is the sum of n random normal elements

$$J_A(\mathbf{x}) = (\mathbf{x} - \mathbf{x}_A)^T \mathbf{S}_A^{-1} (\mathbf{x} - \mathbf{x}_A) = \sum_n \frac{(x_i - x_{Ai})^2}{\sigma_{Ai}^2} \quad (6),$$

and its pdf is given by the Chi-square distribution with n degrees of freedom ($n=3378$ in this case), with an expected value of n and a standard deviation of $\sqrt{2n}$. One can apply the same reasoning to the observation component J_O of the posterior cost function,

$$J_O(\mathbf{x}) = (\mathbf{y} - \mathbf{K}\mathbf{x})^T \mathbf{S}_O^{-1} (\mathbf{y} - \mathbf{K}\mathbf{x}) = \sum_m \frac{(y_i - Kx_i)^2}{\sigma_{oi}^2} \quad (7),$$

whose pdf follows a chi-square distribution with m degrees of freedom. However, this component is less sensitive to the choice of γ because of the large random error component for individual observations.

Figure 4 shows the dependences of $J_A(\hat{\mathbf{x}})$ and $J_O(\hat{\mathbf{x}})$ on the choice of the regularization parameter γ , for the in situ and GOSAT observations. The in situ observations are sufficiently sparse that $\gamma = 1$ (no regularization) is expected. In the case of GOSAT, however, $\gamma = 1$ would yield $J_A(\hat{\mathbf{x}}) = 6n \gg n \pm \sqrt{2n}$ which indicates overfitting, while $\gamma = 0.1$ yields $J_A(\hat{\mathbf{x}}) \approx n$ which is the expected value and is used here. This can be explained by the high observation density of GOSAT, such that error correlation between individual observations through the forward model may be expected and would have a large effect on the solution. Maasackers et al. (2019) found that $\gamma = 0.05$ and $\gamma = 0.1$ gave similar solutions in their global inversions of GOSAT data. We also conduct sensitivity tests using $\gamma = 0.5$ for in situ observations and $\gamma = 0.05$ for GOSAT observations.

The analytical solution to the Bayesian optimization problem, as done here, has several advantages relative to the more commonly used variational (numerical) solution. (1) It finds the true minimum in the cost function, rather than an approximation that may be sensitive to the choice of initial estimate. (2) It identifies the information content of the inversion and the ability to constrain each state vector element. (3) It enables a range of sensitivity analyses, modifying the prior estimates, modifying the error covariance matrices, adding/subtracting observations, etc. at minimal computational cost. We will make use of these

317 advantages in comparing the ability of the in-situ-only, GOSAT-only, and GOSAT + in situ inversions,
 318 and to test how choices in cost-function construction affect our conclusions including changing the
 319 regularization parameter γ , changing the prior error estimates, and using different types of in-situ
 320 observations. Our analysis will focus on results from the base inversions with the default settings, but we
 321 will use results from the sensitivity inversions to address specific issues.

322
 323 A requirement of the analytical approach is that the Jacobian matrix be explicitly constructed, requiring
 324 $n + 1$ forward model runs. Building the Jacobian matrix for the 3378 state vectors in this 8-year period
 325 study requires about one million core hours (8 cores \times 36 hours per simulation \times 3378 simulations).
 326 However, this construction is readily done in parallel on high-performance computing clusters.

327
 328 Our inversion returns posterior emission estimates and their temporal trends on a $4^\circ \times 5^\circ$ grid for non-
 329 wetland emissions, and monthly mean wetland emissions for individual years in 14 subcontinental regions.
 330 We cannot separate individual sectors within a $4^\circ \times 5^\circ$ grid cell because they will all have the same response
 331 function (Jacobian column). However, we can aggregate results spatially and by sector in a way that
 332 retains the error covariance of the solution (Maasackers et al., 2019). Consider a reduced state vector \mathbf{x}_{red}
 333 representing a linear combination of the original state vector elements that may be a sum over a particular
 334 region or the globe, and may be weighted by the contributions from individual sectors following the prior
 335 distribution. The linear transformation from the posterior full-dimension state vector $\hat{\mathbf{x}}$ to the reduced
 336 state vector $\hat{\mathbf{x}}_{red}$ is defined by a summation matrix \mathbf{W}

$$337 \quad \hat{\mathbf{x}}_{red} = \mathbf{W}\hat{\mathbf{x}} \quad (8).$$

338
 339 The posterior error covariance and averaging kernel matrices for the reduced state vector can then be
 340 calculated as:

$$341 \quad \hat{\mathbf{S}}_{red} = \mathbf{W}\hat{\mathbf{S}}\mathbf{W}^T \quad (9),$$

$$342 \quad \mathbf{A}_{red} = \mathbf{W}\mathbf{A}\mathbf{W}^* \quad (10),$$

343 where $\mathbf{W}^* = \mathbf{W}^T(\mathbf{W}\mathbf{W}^T)^{-1}$ (Calisesi et al., 2005). $\hat{\mathbf{S}}_{red}$ provides a means to determine error
 344 correlations between aggregates of quantities optimized by the inversion, e.g., between global methane
 345 emissions and global OH concentrations. \mathbf{A}_{red} provides a means to determine the ability of the inversion
 346 to constrain an aggregated term (e.g., emissions from a particular sector).

347 348 **3. Results and discussion**

349 **3.1 Ability to fit the in situ and GOSAT data**

350 We will present results from three different inversions for 2010-2017: (1) using only in situ observations
 351 (in-situ-only inversion), (2) using only GOSAT observations (GOSAT-only inversion), and (3) using both
 352 GOSAT and in situ observations (GOSAT + in situ inversion). Here we first evaluate the ability of these
 353 different inversions to fit the in situ and GOSAT observations, including when the data are not used in the
 354 inversion (consistency check). This is done by conducting GEOS-Chem simulations with posterior values
 355 for the state vectors and comparing to observations.

356

357 Figures 5 and 6 show the resulting comparisons for the in situ observations, arranged by type of platform
358 (Fig.5), and by latitude bands and months (panels (a)-(d) in Fig.6). The model simulation with prior
359 estimates shows a 30-60 ppb low bias for all in situ platforms growing with time. The in-situ-only
360 inversion effectively corrects this bias and its trend, and also significantly improves the correlations across
361 all platforms. The GOSAT-only inversion performs comparably in correcting the 2010-2017 trend for the
362 independent in-situ data (Fig.6c) and bias for background observations (e.g. aircraft observations in the
363 Southern Hemisphere (Fig.S2)), but there is a low bias at northern mid-latitudes reflecting surface and
364 tower data in North America and Europe. As we will see, the in situ observations are important for
365 optimizing emissions in these regions.

366

367 Figure 6 also compares the fits to the GOSAT observations (panels (e)-(h)). The GOSAT-only inversion
368 corrects the bias and trend in the prior simulation at all latitudes. The in-situ-only inversion corrects the
369 trends, but biases low to the GOSAT observations by about 10 ppbv with larger bias in the Southern
370 Hemisphere due to the sparsity of in situ observation there. The comparison suggests that in situ and
371 GOSAT observations are largely consistent for informing the global methane change but also have some
372 complementarity for the inversion. The GOSAT + in situ joint inversion shows good agreement with both
373 the in situ and GOSAT observations.

374

375 Figure 7a further evaluates the global methane growth rate as determined by the methane budget
376 imbalance for individual years in 2010-2017 from the three inversions. The observed methane growth
377 rate inferred from the NOAA sites (https://www.esrl.noaa.gov/gmd/ccgg/trends_ch4/, last access: 20 June
378 2020) averages 7.2 ± 2.8 ppb a^{-1} over the period, peaking in 2014, and overall accelerating with higher
379 growth in 2015-2017 than in 2010-2013. We find that all posterior simulations show comparable mean
380 methane growth rate (7.7 ± 3.7 ppb a^{-1} for in-situ-only inversion, 8.8 ± 2.2 ppb a^{-1} for GOSAT-only inversion,
381 and 8.3 ± 1.8 ppb a^{-1} for the GOSAT + in situ inversion). However, the in-situ-only inversion overestimates
382 the increasing trend in the methane growth rate, largely driven by the year 2017, and fails to fit its
383 interannual variability. This may reflect the heavy weighting of the in situ observations toward northern
384 mid-latitudes. GOSAT observations in the inversion do much better in capturing the observed methane
385 interannual variability and trend. Adding in situ observations to GOSAT observations provides a better fit
386 in 2015 than GOSAT-only inversion but has an insignificant effect in other years. Zhang et al. (2020a)
387 interpreted the trend and interannual variability in the GOSAT-only inversion as due to a combination of
388 anthropogenic emissions, wetlands, and OH concentrations.

389

390 **3.2 Anthropogenic methane emissions**

391 Figure 8 shows the averaging kernel sensitivities (diagonal elements of the averaging kernel matrix) and
392 posterior scaling factors for the non-wetland emissions (dominated by anthropogenic emissions) in the
393 in-situ-only, GOSAT-only, and GOSAT + in situ joint inversions. The DOFS (trace of the averaging kernel
394 matrix) quantify the number of independent pieces of information from the inversion, starting from 1009

395 unknowns for anthropogenic emissions (Figure 1). The DOFS are 113 for the in-situ-only inversion, 212
396 for the GOSAT-only inversion, and 262 for the GOSAT + in situ joint inversion. The higher DOFS from
397 the joint inversion indicate that the satellite and in situ observations have complementarity but also some
398 redundancy. Strict complementarity would imply a DOFS of $325=113+212$. We find that 75% of the in
399 situ information is at northern mid-latitudes ($30-60^{\circ}\text{N}$, DOFS=82, calculated as the sum of averaging
400 kernel sensitivities in that latitude band) where the observations are densest, with another 9% (DOFS=10)
401 at $60-90^{\circ}\text{N}$. GOSAT provides more information than do in situ observations at northern mid-latitudes
402 (DOFS=96) and dominates in the tropics (DOFS=105). This dominance of satellites for informing
403 methane sources in the tropics has been pointed out in previous studies (Bergamaschi et al., 2013; Monteil
404 et al., 2013; Fraser et al., 2013; Alexe et al., 2015). We find that the DOFS from the in-situ-only inversion
405 observations are mostly (85%) from the surface and tower measurements (Fig.S3).

406
407 We investigate further the inversion results for northern mid-latitudes where most of the information of
408 in situ observations is contained including for the US, Canada, Europe, and China. Table 2 gives the
409 optimization of anthropogenic methane emissions (calculated as the difference between total non-wetland
410 emissions and the non-wetland natural emissions) in these regions. Figure 9 shows the optimization by
411 source sectors, assuming that (1) the partitioning between sectors of non-wetland emissions in individual
412 grid cells is correct in the prior inventory (this does not assume that the prior distribution of sectoral
413 emissions is correct), (2) the scaling factors are to be applied equally to all sectors in a grid cell. These
414 assumptions are adequate when the sectors are spatially separated but are more prone to error when they
415 spatially overlap. Figure 9 also shows the averaging kernel sensitivities of emission sectors (diagonal
416 terms of A_{red} derived from Equations (8) and (10)), measuring the ability of the inversion to optimize
417 different emissions sectors, and the DOFS for each inversion summed over the region. Wetland methane
418 emissions are optimized separately as will be discussed in Section 3.3.

419
420 Inspection of the DOFS shows that the in situ observations are more effective than GOSAT for optimizing
421 US anthropogenic methane emissions (DOFS=41 vs. DOFS=22) and this applies to all sectors (Figure 9).
422 The averaging kernel sensitivities panel in Figure 9 shows that US results from the joint GOSAT + in situ
423 inversion are mostly determined by the in situ observations. The joint GOSAT + in situ inversion increases
424 anthropogenic US emissions from 28 Tg a^{-1} in the prior EPA GHGI to 36 Tg a^{-1} , with most of the increase
425 driven by oil/gas sources in the central US. Averaging kernel sensitivity for major sectors is large (0.63-
426 0.93), indicating that the posterior estimates are mostly determined by the observations rather than by the
427 prior estimates. The underestimate of oil/gas emissions in the EPA GHGI has been reported before in
428 local observations and higher-resolution inversions (Miller et al., 2013; Turner et al., 2015; Alvarez et al.,
429 2018; Cui et al., 2019; Maasackers et al., 2020).

430
431 The in situ observations are also more effective than GOSAT in optimizing anthropogenic methane
432 emissions in Canada (DOFS=21 vs. DOFS=6), particularly in Alberta where oil/gas emissions are high
433 (Fig.8). This reflects in part our exclusion of GOSAT data poleward of 60°N . Oil/gas emissions in Canada

434 increase by a factor of 2 in the GOSAT + in situ inversion to 4.5 Tg a⁻¹ compared to UNFCCC prior
435 estimate, with an averaging kernel sensitivity of 0.57 (Fig.9). Total anthropogenic emissions increase
436 from 5 Tg a⁻¹ to 8 Tg a⁻¹.

437
438 In situ and GOSAT observations show comparable ability in optimizing the total anthropogenic emissions
439 in Europe (DOFS=16~18). They agree that prior anthropogenic methane emissions are too high in
440 northern Europe but disagree in southern Europe. Averaging kernel sensitivities from the insitu-only
441 inversion are slightly weaker than for the US and Canada because of the lower density of in situ sites. The
442 Integrated Carbon Observation system (ICOS) network (<https://www.icos-cp.eu/>, last access: 17 July
443 2020) has increased substantially the number of available methane observations in Europe since 2017 so
444 that future inversions should expect a stronger constraint from in situ observations. Total European
445 anthropogenic emissions decrease from 27 Tg a⁻¹ to 23 Tg a⁻¹ in the GOSAT + in situ joint inversion, with
446 decreases for all sectors but this may reflect the inability of our 4°× 5° resolution to effectively separate
447 emission sectors.

448
449 The only other region where in situ observations provide significant information is China, though the
450 corresponding DOFS=13 is less than for GOSAT (DOFS=22). Both inversions agree that emissions must
451 be greatly decreased from the prior estimate, and the joint inversion (DOFS=28) has stronger power in
452 doing so. The posterior 2010-2017 Chinese anthropogenic emission is 43 Tg a⁻¹ in the joint inversion,
453 compared to 63 Tg a⁻¹ in the prior estimate. Our results agree with a recent study by Janardanan et al.
454 (2020), which also used GOSAT and surface observations to estimate a mean 2011-2017 anthropogenic
455 methane emission in China of 46±9 Tg a⁻¹. The downward correction is mainly driven by a 40% decrease
456 in coal emissions from 19 Tg a⁻¹ to 11 Tg a⁻¹ (Fig. 9). Previous inversions using the EDGAR inventory
457 (>20 Tg a⁻¹) as prior estimate found a similar correction (Alexe et al., 2015; Thompson et al., 2015; Turner
458 et al., 2015; Maasakkers et al., 2019; Miller et al., 2019). In our case, the prior estimate of coal emissions
459 (19 Tg a⁻¹) is the value reported by China to the UNFCCC and we find that it is still too high. A recent
460 inventory by Sheng et al. (2019) gives a coal emission estimate of 15 Tg a⁻¹ for China in 2010-2016.

461 462 **3.3 Wetland methane emissions**

463 The inversion optimizes wetland emissions for the 14 regions of Figure 3 and for 96 individual months
464 covering 2010-2017, amounting to 1344 state vector elements. Results from the in-situ-only, GOSAT-
465 only, and GOSAT + in situ inversions yield DOFS of 221, 183, and 301 respectively. In situ observations
466 provide more information for boreal wetlands while GOSAT dominates for tropical wetlands.

467
468 Zhang et al. (2020a) give a detailed analysis of GOSAT-only inversion results for tropical wetlands. Here
469 we analyzed further the boreal/temperate North America wetlands, where in situ observations provide
470 significant added information (Figure 10). Both in situ and GOSAT observations agree that the prior
471 WetCHARTs emissions are too high. The posterior estimates from the GOSAT + in situ inversion are 4.5
472 and 2.0 Tg a⁻¹ for boreal and temperate North America, respectively, compared to 12.8 and 6.9 Tg a⁻¹ in

473 WetCHARTs. Posterior boreal wetland CH₄ emissions for North America are on the lower end but within
474 the WetCHARTs estimates (WetCHARTs models range 3~33 Tg a⁻¹); however, posterior temperate CH₄
475 emissions for North America are outside the WetCHARTs range (3~12 Tg a⁻¹). The correction for boreal
476 North America is particularly large in May-June, which can potentially be attributed to suppression of
477 wetland emissions by either snow cover (Pickett-Heaps et al., 2011) or frozen soils (Zona et al., 2016).
478 The WetCHARTs emission overestimate for temperate North America (mainly coastal wetlands in the
479 eastern US) has been reported before from inversions using aircraft data (Sheng et al., 2018) and GOSAT
480 data (Maasakkers et al., 2020).

481

482 **3.4 Anthropogenic methane emission trends**

483 Figure 11 presents the 2010-2017 trends (% a⁻¹) of anthropogenic methane emissions from the three
484 inversions, and the corresponding averaging kernel sensitivities. The GOSAT + in situ inversion has a
485 DOFS = 161 for quantifying the spatial distribution of the trends. Most of that information is from GOSAT
486 (DOFS = 122) but in situ observations add significant information. Information from in situ observations
487 is concentrated in the US, Canada, Europe, and China. Table 2 summarizes the trends for the four regions.
488 Figure 12 shows the trends disaggregated by sectors, using the same procedure as for Figure 9.

489

490 In situ observations provide stronger constraints than GOSAT on anthropogenic emission trends in the
491 US (DOFS=29 vs. DOFS=12). They agree on the upward trend in the eastern US as also found in
492 Maasakkers et al. (2020) which used GOSAT in a high resolution inversion to interpret methane trends in
493 the US in 2010-2015. However, they show opposite trends (positive trend from in-situ-only inversion but
494 negative from GOSAT-only inversion) in total emissions and in the central south US (Table 2, Fig. 11).
495 The GOSAT + in situ joint inversion (DOFS=31) estimates that US anthropogenic methane emissions
496 increased by 0.4 Tg a⁻¹ a⁻¹ (1.1% a⁻¹) from 2010 to 2017, with the largest contribution from oil/gas
497 emissions (0.3 Tg a⁻¹ a⁻¹, 2.5% a⁻¹). This posterior trend is much smaller than previous studies showing
498 large increases in US oil/gas emissions (2.1–4.4 Tg a⁻¹ a⁻¹) inferred from ethane/propane levels (Franco
499 et al., 2016; Hausmann et al., 2016; Helmig et al., 2016), but is more consistent with a recent study by
500 Lan et al. (2019) of 0.3±0.1 Tg a⁻¹ a⁻¹ in 2006-2015 based on long-term in situ measurements. The
501 inversion also reveals rising emissions from oil/gas in the central south US, including the Permian Basin
502 which is currently the largest oil-producing basin in the US (Zhang et al., 2020b).

503

504 We find that anthropogenic emissions in Canada decrease over the 2010-2017 period by 0.2 Tg a⁻¹ a⁻¹
505 (2.5% a⁻¹) in the GOSAT + in situ joint inversion, mostly driven by oil/gas emissions in Alberta and
506 livestock emissions (Figs. 11-12). Anthropogenic emissions in Europe decrease by 0.4 Tg a⁻¹ a⁻¹ (1.7 % a⁻¹)
507 ¹).

508

509 All three inversions show increases of Chinese anthropogenic methane emissions over 2010-2017 by 0.1-
510 0.4 Tg a⁻¹ a⁻¹ (0.3-0.9% a⁻¹), but the spatial patterns and source attributions are different. The largest
511 difference is for coal mining emissions in the North China Plain, where in situ observations indicate a

512 decrease of $-0.8 \text{ Tg a}^{-1} \text{ a}^{-1}$ while GOSAT shows an increase of $0.1 \text{ Tg a}^{-1} \text{ a}^{-1}$. A previous GOSAT inversion
513 study found a large increase of coal mining emissions in China over 2010-2015 (Miller et al., 2019).
514 However, a recent bottom-up inventory estimates that Chinese coal emission peaked in 2012 and
515 decreased afterward, leading to no significant overall trend for 2010-2016 (Sheng et al., 2019). Our
516 inversion assumes linear trends in emissions over 2010-2017 but that may not be appropriate for China.

517 **3.5 Global methane budget for 2010-2017**

518 Table 1 shows the optimized global anthropogenic emissions from different sectors as determined by the
519 joint GOSAT + in situ inversion. Corrections to the global prior estimates are mostly determined by
520 GOSAT (Fig. 8). They include upward corrections to livestock and rice methane emissions, and
521 downward correction to the coal mining emissions driven by overestimation in China. The joint inversion
522 also estimates a global increase in anthropogenic emissions by $1.7 \pm 0.6 \text{ Tg a}^{-1} \text{ a}^{-1}$ ($0.5\% \text{ a}^{-1}$) in 2010-2017,
523 dominantly driven by trends in the tropics (Fig. 11).

524
525
526 A number of previous studies have analyzed surface observations to interpret global methane budgets and
527 trends (Dlugokencky et al., 2009; Bruhwiler et al., 2014; Houweling et al., 2017). As shown in Figure 6,
528 our in-situ-only inversion can fit the GOSAT observations of global methane distribution and trend,
529 indicating that the in situ data provide useful information on the global budget. Here we examine whether
530 this information adds to that from GOSAT. For this purpose and following Maasakkers et al. (2019), we
531 collapse the full state vector to a reduced state vector ($\hat{\mathbf{x}}_{red}$) that contains global mean methane emissions
532 and OH as elements, and derive the associated error covariance matrix ($\hat{\mathbf{S}}_{red}$) as introduced in Section
533 2.4.

534
535 Figure 13 shows the joint probability density functions (PDFs) of the mean anthropogenic methane
536 emissions and methane lifetime against oxidation by tropospheric OH from the three inversions. There is
537 strong negative correlation ($r=-0.72$) between the optimization of methane emissions and OH in the
538 GOSAT-only inversion, and somewhat less in the in-situ-only inversion ($r=-0.53$), although the posterior
539 error variance is larger due to the lower data density as indicated by the axes of the ellipses. A sensitivity
540 inversion using only the surface and tower measurements in the in-situ-only inversion yields $r=-0.37$
541 (Fig.13b). It indicates that in situ observations, in particular surface and tower measurements, are more
542 effective than the satellite observations in constraining methane emissions independently from the sink
543 by OH. A likely reason is that surface measurements in source regions are more sensitive to methane
544 emissions than are column measurements. We also find that the in-situ-only inversion yields a larger
545 interannual variability of posterior OH concentrations and thus methane lifetime than the GOSAT-only
546 inversion (Fig.7b and Fig.S4). This is because the number and location of the observations varies from
547 year to year, particularly for aircraft campaigns and ship cruises., due to the heterogeneous spatial and
548 temporal distribution of the in-situ observations.

549
550 Comparison of the posterior PDFs between the GOSAT-only and in-situ-only inversions implies that the

551 two are inconsistent in optimizing global methane budgets, since the 99% probability contours do not
552 overlap (Fig. 13a). A possible cause is that the posterior error covariance matrix underestimates the actual
553 error variance due to its assumption of independent identically distributed (IID) observational errors
554 (Brasseur and Jacob, 2017), and this would particularly affect the global budget which sums emission
555 results for individual grid cells. Remarkably, the solution from the GOSAT + in situ joint inversion is
556 more in agreement with in situ observations than GOSAT, and does not lie between these two solutions.
557 Inspection of Figure 6c shows that the GOSAT-only inversion is biased low relative to in situ observations
558 at northern mid-latitudes and biased high in the southern hemisphere, implying that both emissions and
559 OH concentrations are too low. On the other hand, Figure 6f indicates either underestimation of emissions
560 or overestimation of OH concentrations in the in-situ-only inversion, and the former one is more likely as
561 GOSAT measurements used here are over land which should be more sensitive to emissions than OH loss.
562 Ingestion of both observations in the GOSAT + in situ inversion thus enhances both the methane emissions
563 and OH concentrations compared to the in-situ-only and GOSAT-only inversion to correct these biases.
564 It also narrows the posterior error of mean anthropogenic emissions and methane lifetime against
565 tropospheric OH by 20% and 50% compared to the GOSAT-only and in-situ-only inversions, respectively
566 (Fig. 13a). Thus we find that the GOSAT and in situ observations are complementary in quantifying the
567 global budget.

568
569 Table 3 summarizes the global mean methane budget in 2010-2017. The GOSAT + in situ joint inversion
570 estimates a total methane emission of 551 Tg a⁻¹, of which 371 Tg a⁻¹ are anthropogenic, and a total sink
571 of 529 Tg a⁻¹. The total emission is within the 550-594 Tg a⁻¹ range of top-down estimates but lower than
572 the 594-881 Tg a⁻¹ range of bottom-up estimates reported for the 2008-2017 decade by the Global Carbon
573 Project (Saunois et al., 2020). Our joint inversion yields a methane lifetime against OH oxidation of 11.2
574 years, consistent with the observationally-based estimate of 11.2±1.3 years (Prather et al., 2012), and
575 pushes the northern to southern hemispheric OH ratio (1.06 in GOSAT + in situ inversion versus 1.16 in
576 prior estimate) closer to the values of 0.97±0.12 inferred from methyl chloroform observations (Patra et
577 al., 2014).

578
579 We examine in Figure 13b the sensitivity of the global methane budget optimization to the choice of
580 different regularization parameter γ (and therefore observation error \mathbf{S}_0) and prior error of methane
581 emission trends and OH concentrations. We find that reducing γ or prior errors of trend and OH by 50%
582 yields consistent estimates of anthropogenic emissions and OH concentrations as compared to the default
583 inversion, with differences within 3%. Decreasing the weighting of observations in the inversion (i.e.
584 assuming larger observation error) enlarges the posterior error and pushes the posterior estimates closer
585 to the prior estimates. Assuming a lower prior error for OH concentration from 10% to 5% results in lower
586 methane lifetime (closer to the prior) and higher emissions, and also reduces the error correlation between
587 the optimization of methane emissions and OH, while assuming a lower prior error for non-wetland
588 emission trends leads to an opposite effect. Our results are consistent with Maasakkers et al. (2019), which
589 shows that different assumptions of error distribution and magnitude in their analyses have relatively

590 small results. We also find that having the shipboard and aircraft measurements in the in-situ-only
591 inversion pushes the estimate to be more consistent with the GOSAT-only inversion (Fig.13b), implying
592 that the shipboard and aircraft measurements by emphasizing the methane in the remote atmosphere play
593 a similar role as satellite measurements in global methane budget optimization.

594

595 **4 Conclusions**

596 We quantified and attributed global sources, sinks, and trends of atmospheric methane for 2010-2017 by
597 inversions of GOSAT satellite data and the GLOBALVIEWplus in situ methane observations from surface
598 sites, towers, ships, and aircraft. The inversions use an analytical solution to Bayesian optimization
599 problem including closed-form error covariance matrices from which the detailed information content of
600 the inversion can be derived. We conduct inversions using GOSAT and in situ data separately and
601 combined. In this manner we are able to quantify the consistency and complementarity (or redundancy)
602 of the satellite and in situ observations.

603

604 We find that the GOSAT-only inversion can generally fit the in situ data and the in-situ-only inversion
605 can generally fit the GOSAT data, indicating consistency between the two data sets. However, the
606 GOSAT-only inversion has difficulty fitting the in situ observations in source regions (US and Europe),
607 while -the in-situ-only inversion cannot reproduce the interannual variability of the methane growth rate
608 due to the heavy weighting of in situ data to northern mid-latitudes. The GOSAT + in situ inversion shows
609 the best fit to the ensemble of observations.

610

611 GOSAT and in situ observations have complementarity in constraining global emissions. GOSAT
612 provides stronger constraints than in situ observations for the tropics, while in situ observations are more
613 important in the US, Canada, Europe, and northern China where observations are most dense. The
614 GOSAT-only and in-situ-only inversions also show consistent corrections to regional methane emissions
615 in the US, Europe, and China. The joint GOSAT + in situ inversion indicates large underestimates of
616 oil/gas emissions in the US and Canada, and large overestimates of coal emissions in China, relative to
617 the national inventories reported to the United Nations Framework Convention on Climate Change
618 (UNFCCC) and used here as prior estimates for our inversions. Emissions from boreal wetlands are
619 overestimated in the mean WetCHARTs inventory used as prior estimate, particularly in May-June when
620 snow cover and frozen soils inhibit methane emission.

621

622 Our inversions indicate increasing trends in US anthropogenic emissions driven by oil/gas production but
623 decreasing trends in Canada (oil/gas) and Europe. Joint inversion of GOSAT + in situ data shows a weak
624 decreasing trend in Chinese coal emissions for 2010-2017, consistent with a recent bottom-up inventory
625 (Sheng et al., 2019).

626

627 We find that GOSAT and in situ observations are also complementary in constraining the global methane
628 budget. While the global budget information relies more on GOSAT observations, information from the

629 in situ observations at northern mid-latitudes avoids the large error correlations between methane
630 emissions and sink from OH and also corrects the underestimation of both emission and OH in the
631 GOSAT-only inversion. Our joint GOSAT + in situ inversion yields global methane emissions and loss of
632 551 and 529 Tg a⁻¹ a⁻¹ averaged over 2010-2017, and a methane lifetime of 11.2 years.

633

634 Our study presents a framework to integrate satellite and in situ data in analytical inversions. We conclude
635 that on the basis of the present observation system, in situ and satellite observations are complementary
636 for constraining global methane budgets and regional emissions. Satellite observations of atmospheric
637 methane are presently expanding with the new availability of global daily data from the TROPOMI
638 instrument launched in October 2017 (Hu et al., 2018). This will call for re-evaluating the role of in situ
639 observations for constraining regional and global methane budgets, as can be done with the methods
640 presented here. In situ observations will in any case continue to play a critical role for documenting long-
641 term trends of methane with consistent calibration, for observation of oceanic and polar regions where
642 satellites have limited capability, for high-frequency measurements in source regions giving insight into
643 the magnitude and intermittency of local emissions, and for independent validation of satellite-based
644 inversions.

645

646 **Data availability**

647 The GLOBALVIEWplus CH₄ ObsPack v1.0 data product is available at
648 https://www.esrl.noaa.gov/gmd/ccgg/obspack/data.php?id=obspack_ch4_1_GLOBALVIEWplus_v1.0_2019-01-08 (last access: July 17, 2020). The GOSAT proxy satellite methane observations are available
649 at <https://doi.org/10.5285/18ef8247f52a4cb6a14013f8235cc1eb> (last access: July 17, 2020). Modeling
650 data can be accessed by contacting the corresponding authors Xiao Lu (xiaolu@g.harvard.edu) and
651 Yuzhong Zhang (zhangyuzhong@westlake.edu.cn).

653

654 **Author contributions**

655 XL and DJJ designed the study. XL and YZZ conducted the modeling and data analyses with contributions
656 from JDM, MPS, LS, ZQ, TRS, HON, RMY, and JXS. AA contributed to the GLOBALVIEWplus CH₄
657 ObsPack v1.0 data product. RJP and HB contributed to the GOSAT satellite methane retrievals. AAB and
658 SM contributed to the WetCHARTs wetland emission inventory and its interpretation. XL and DJJ wrote
659 the paper with input from all authors.

660

661 **Competing interests**

662 The authors declare that they have no conflict of interest.

663

664 **Acknowledgement**

665 This work was supported by the NOAA AC4 program. RJP and HB are funded via the UK National Centre
666 for Earth Observation (NCEO grant numbers: NE/R016518/1 and NE/N018079/1). RJP and HB
667 acknowledge funding from the ESA GHG-CCI and Copernicus C3S projects. We thank the Japanese

668 Aerospace Exploration Agency, National Institute for Environmental Studies, and the Ministry of
669 Environment for the GOSAT data and their continuous support as part of the Joint Research Agreement.
670 This research used the ALICE High Performance Computing Facility at the University of Leicester for
671 the GOSAT retrievals. Part of this research was carried out at the Jet Propulsion Laboratory, California
672 Institute of Technology, under a contract with the National Aeronautics and Space Administration.

673
674 We acknowledge all data providers/laboratories (<https://search.datacite.org/works/10.25925/20190108>)
675 contributed to the GLOBALVIEWplus CH₄ ObsPack v1.0 data product compiled by NOAA Global
676 Monitoring Laboratory. We acknowledge methane observations collected from the CONTRAIL
677 (Comprehensive Observation Network for TRace gases by AIrLiner) project (Machida et al., 2019). Data
678 collected at WLEF Park Falls towers were supported by the NSF DEB-0845166 and DOE Ameriflux
679 Network Management Project. Data collected at the Southern Great Plains were supported by the Office
680 of Biological and Environmental Research of the US Department of Energy under contract no. DE-AC02-
681 05CH11231 as part of the Atmospheric Radiation Measurement (ARM) Program, ARM Aerial Facility
682 (AAF), and Terrestrial Ecosystem Science (TES) Program.

683

684 Reference

- 685 Alexe, M., Bergamaschi, P., Segers, A., Detmers, R., Butz, A., Hasekamp, O., Guerlet, S., Parker, R., Boesch, H., Frankenberg,
686 C., Scheepmaker, R. A., Dlugokencky, E., Sweeney, C., Wofsy, S. C., and Kort, E. A.: Inverse modelling of CH₄ emissions
687 for 2010–2011 using different satellite retrieval products from GOSAT and SCIAMACHY, *Atmos. Chem. Phys.*, 15, 113-
688 133, <http://doi.org/10.5194/acp-15-113-2015>, 2015.
- 689 Alvarez, R. A., Zavala-Araiza, D., Lyon, D. R., Allen, D. T., Barkley, Z. R., Brandt, A. R., Davis, K. J., Herndon, S. C., Jacob,
690 D. J., Karion, A., Kort, E. A., Lamb, B. K., Lauvaux, T., Maasackers, J. D., Marchese, A. J., Omara, M., Pacala, S. W.,
691 Peischl, J., Robinson, A. L., Shepson, P. B., Sweeney, C., Townsend-Small, A., Wofsy, S. C., and Hamburg, S. P.:
692 Assessment of methane emissions from the U.S. oil and gas supply chain, *Science*, 361, 186-188,
693 <http://doi.org/10.1126/science.aar7204>, 2018.
- 694 Bergamaschi, P., Frankenberg, C., Meirink, J. F., Krol, M., Dentener, F., Wagner, T., Platt, U., Kaplan, J. O., Körner, S.,
695 Heimann, M., Dlugokencky, E. J., and Goede, A.: Satellite cartography of atmospheric methane from SCIAMACHY on
696 board ENVISAT: 2. Evaluation based on inverse model simulations, *J. Geophys. Res.*, 112,
697 <http://doi.org/10.1029/2006jd007268>, 2007.
- 698 Bergamaschi, P., Frankenberg, C., Meirink, J. F., Krol, M., Villani, M. G., Houweling, S., Dentener, F., Dlugokencky, E. J.,
699 Miller, J. B., Gatti, L. V., Engel, A., and Levin, I.: Inverse modeling of global and regional CH₄ emissions using
700 SCIAMACHY satellite retrievals, *J. Geophys. Res.*, 114, <http://doi.org/10.1029/2009jd012287>, 2009.
- 701 Bergamaschi, P., Houweling, S., Segers, A., Krol, M., Frankenberg, C., Scheepmaker, R. A., Dlugokencky, E., Wofsy, S. C.,
702 Kort, E. A., Sweeney, C., Schuck, T., Brenninkmeijer, C., Chen, H., Beck, V., and Gerbig, C.: Atmospheric CH₄ in the
703 first decade of the 21st century: Inverse modeling analysis using SCIAMACHY satellite retrievals and NOAA surface
704 measurements, *J. Geophys. Res.*, 118, 7350-7369, <http://doi.org/10.1002/jgrd.50480>, 2013.
- 705 Bey, I., Jacob, D. J., Yantosca, R. M., Logan, J. A., Field, B. D., Fiore, A. M., Li, Q., Liu, H. Y., Mickley, L. J., and Schultz,
706 M. G.: Global modeling of tropospheric chemistry with assimilated meteorology: Model description and evaluation, *J.*
707 *Geophys. Res.*, 106, 23073-23095, <http://doi.org/10.1029/2001jd000807>, 2001.
- 708 Bloom, A. A., Bowman, K. W., Lee, M., Turner, A. J., Schroeder, R., Worden, J. R., Weidner, R., McDonald, K. C., and Jacob,
709 D. J.: A global wetland methane emissions and uncertainty dataset for atmospheric chemical transport models
710 (WetCHARTs version 1.0), *Geoscientific Model Development*, 10, 2141-2156, <http://doi.org/10.5194/gmd-10-2141-2017>,

711 2017.

712 Bousquet, P., Ringeval, B., Pison, I., Dlugokencky, E. J., Brunke, E. G., Carouge, C., Chevallier, F., Fortems-Cheiney, A.,
713 Frankenberg, C., Hauglustaine, D. A., Krummel, P. B., Langenfelds, R. L., Ramonet, M., Schmidt, M., Steele, L. P., Szopa,
714 S., Yver, C., Viovy, N., and Ciais, P.: Source attribution of the changes in atmospheric methane for 2006–2008, *Atmos.*
715 *Chem. Phys.*, 11, 3689-3700, <http://doi.org/10.5194/acp-11-3689-2011>, 2011.

716 Brasseur, G. P., and Jacob, D. J.: *Modeling of Atmospheric Chemistry*, Cambridge University Press,
717 <http://doi.org/10.1017/9781316544754>, 2017.

718 Bruhwiler, L., Dlugokencky, E., Masarie, K., Ishizawa, M., Andrews, A., Miller, J., Sweeney, C., Tans, P., and Worthy, D.:
719 CarbonTracker-CH4: an assimilation system for estimating emissions of atmospheric methane, *Atmos. Chem. Phys.*, 14,
720 8269-8293, <http://doi.org/10.5194/acp-14-8269-2014>, 2014.

721 Bruhwiler, L. M., Basu, S., Bergamaschi, P., Bousquet, P., Dlugokencky, E., Houweling, S., Ishizawa, M., Kim, H. S., Locatelli,
722 R., Maksyutov, S., Montzka, S., Pandey, S., Patra, P. K., Petron, G., Saunio, M., Sweeney, C., Schwietzke, S., Tans, P.,
723 and Weatherhead, E. C.: U.S. CH₄ emissions from oil and gas production: Have recent large increases been detected?, *J.*
724 *Geophys. Res.*, 122, 4070-4083, <http://doi.org/10.1002/2016jd026157>, 2017.

725 Buchwitz, M., Reuter, M., Schneising, O., Boesch, H., Guerlet, S., Dils, B., Aben, I., Armante, R., Bergamaschi, P.,
726 Blumenstock, T., Bovensmann, H., Brunner, D., Buchmann, B., Burrows, J. P., Butz, A., Chédin, A., Chevallier, F.,
727 Crevoisier, C. D., Deutscher, N. M., Frankenberg, C., Hase, F., Hasekamp, O. P., Heymann, J., Kaminski, T., Laeng, A.,
728 Lichtenberg, G., De Mazière, M., Noël, S., Notholt, J., Orphal, J., Popp, C., Parker, R., Scholze, M., Sussmann, R., Stiller,
729 G. P., Warneke, T., Zehner, C., Bril, A., Crisp, D., Griffith, D. W. T., Kuze, A., O'Dell, C., Oshchepkov, S., Sherlock, V.,
730 Suto, H., Wennberg, P., Wunch, D., Yokota, T., and Yoshida, Y.: The Greenhouse Gas Climate Change Initiative (GHG-
731 CCI): Comparison and quality assessment of near-surface-sensitive satellite-derived CO₂ and CH₄ global data sets,
732 *Remote Sens. Environ.*, 162, 344-362, <http://doi.org/10.1016/j.rse.2013.04.024>, 2015.

733 Butz, A., Guerlet, S., Hasekamp, O., Schepers, D., Galli, A., Aben, I., Frankenberg, C., Hartmann, J. M., Tran, H., Kuze, A.,
734 Keppel-Aleks, G., Toon, G., Wunch, D., Wennberg, P., Deutscher, N., Griffith, D., Macatangay, R., Messerschmidt, J.,
735 Notholt, J., and Warneke, T.: Toward accurate CO₂ and CH₄ observations from GOSAT, *Geophys. Res. Lett.*, 38, n/a-n/a,
736 <http://doi.org/10.1029/2011gl047888>, 2011.

737 Calisesi, Y., Soebijanta, V. T., and van Oss, R.: Regridding of remote soundings: Formulation and application to ozone profile
738 comparison, *J. Geophys. Res.*, 110, <http://doi.org/10.1029/2005jd006122>, 2005.

739 Cooperative Global Atmospheric Data Integration Project: Multi-laboratory compilation of atmospheric methane data for the
740 period 1957-2017; obspack_ch4_1_GLOBALVIEWplus_v1.0_2019_01_08; NOAA Earth System Research Laboratory,
741 Global Monitoring Laboratory. <http://dx.doi.org/10.25925/20190108>, 2019

742 Cressot, C., Chevallier, F., Bousquet, P., Crevoisier, C., Dlugokencky, E. J., Fortems-Cheiney, A., Frankenberg, C., Parker, R.,
743 Pison, I., Scheepmaker, R. A., Montzka, S. A., Krummel, P. B., Steele, L. P., and Langenfelds, R. L.: On the consistency
744 between global and regional methane emissions inferred from SCIAMACHY, TANSO-FTS, IASI and surface
745 measurements, *Atmos. Chem. Phys.*, 14, 577-592, <http://doi.org/10.5194/acp-14-577-2014>, 2014.

746 Cui, Y. Y., Henze, D. K., Brioude, J., Angevine, W. M., Liu, Z., Bousserez, N., Guerrette, J., McKeen, S. A., Peischl, J., Yuan,
747 B., Ryerson, T., Frost, G., and Trainer, M.: Inversion Estimates of Lognormally Distributed Methane Emission Rates
748 From the Haynesville-Bossier Oil and Gas Production Region Using Airborne Measurements, *J. Geophys. Res.*, 124,
749 3520-3531, <http://doi.org/10.1029/2018jd029489>, 2019.

750 Cusworth, D. H., Jacob, D. J., Sheng, J.-X., Benmergui, J., Turner, A. J., Brandman, J., White, L., and Randles, C. A.: Detecting
751 high-emitting methane sources in oil/gas fields using satellite observations, *Atmos. Chem. Phys.*, 18, 16885-16896,
752 <http://doi.org/10.5194/acp-18-16885-2018>, 2018.

753 Dlugokencky, E. J., Steele, L. P., Lang, P. M., and Masarie, K. A.: The growth rate and distribution of atmospheric
754 methane, *J. Geophys. Res.*, 99, 17021, <http://doi.org/10.1029/94jd01245>, 1994.

755 Dlugokencky, E. J., Bruhwiler, L., White, J. W. C., Emmons, L. K., Novelli, P. C., Montzka, S. A., Masarie, K. A., Lang, P. M.,

756 Crotwell, A. M., Miller, J. B., and Gatti, L. V.: Observational constraints on recent increases in the atmospheric
757 CH₄ burden, *Geophys. Res. Lett.*, 36, <http://doi.org/10.1029/2009gl039780>, 2009.

758 Etiope, G., Ciotoli, G., Schwietzke, S., and Schoell, M.: Gridded maps of geological methane emissions and their isotopic
759 signature, *Earth System Science Data*, 11, 1-22, <http://doi.org/10.5194/essd-11-1-2019>, 2019.

760 Franco, B., Mahieu, E., Emmons, L. K., Tzompa-Sosa, Z. A., Fischer, E. V., Sudo, K., Bovy, B., Conway, S., Griffin, D.,
761 Hannigan, J. W., Strong, K., and Walker, K. A.: Evaluating ethane and methane emissions associated with the development
762 of oil and natural gas extraction in North America, *Environmental Research Letters*, 11, 044010,
763 <http://doi.org/10.1088/1748-9326/11/4/044010>, 2016.

764 Fraser, A., Palmer, P. I., Feng, L., Boesch, H., Cogan, A., Parker, R., Dlugokencky, E. J., Fraser, P. J., Krummel, P. B.,
765 Langenfelds, R. L., and Doherty, S., Prinn, R. G., Steele, L. P., van der Schoot, M., and Weiss, R. F.: Estimating
766 regional methane surface fluxes: the relative importance of surface and GOSAT mole fraction measurements, *Atmos.*
767 *Chem. Phys.*, 13, 5697-5713, <http://doi.org/10.5194/acp-13-5697-2013>, 2013.

768 Fung, I., John, J., Lerner, J., Matthews, E., Prather, M., Steele, L. P., and Fraser, P. J.: Three-dimensional model synthesis of
769 the global methane cycle, *J. Geophys. Res.*, 96, 13033, <http://doi.org/10.1029/91jd01247>, 1991.

770 Ganesan, A. L., Rigby, M., Lunt, M. F., Parker, R. J., Boesch, H., Goulding, N., Umezawa, T., Zahn, A., Chatterjee, A., Prinn,
771 R. G., Tiwari, Y. K., van der Schoot, M., and Krummel, P. B.: Atmospheric observations show accurate reporting and little
772 growth in India's methane emissions, *Nat Commun*, 8, 836, <http://doi.org/10.1038/s41467-017-00994-7>, 2017.

773 Gelaro, R., McCarty, W., Suárez, M. J., Todling, R., Molod, A., Takacs, L., Randles, C. A., Darmenov, A., Bosilovich, M. G.,
774 Reichle, R., Wargan, K., Coy, L., Cullather, R., Draper, C., Akella, S., Buchard, V., Conaty, A., da Silva, A. M., Gu, W.,
775 Kim, G.-K., Koster, R., Lucchesi, R., Merkova, D., Nielsen, J. E., Partyka, G., Pawson, S., Putman, W., Rienecker, M.,
776 Schubert, S. D., Sienkiewicz, M., and Zhao, B.: The Modern-Era Retrospective Analysis for Research and Applications,
777 Version 2 (MERRA-2), *J. Clim.*, 30, 5419-5454, <http://doi.org/10.1175/jcli-d-16-0758.1>, 2017.

778 Hausmann, P., Sussmann, R., and Smale, D.: Contribution of oil and natural gas production to renewed increase in atmospheric
779 methane (2007–2014): top–down estimate from ethane and methane column observations, *Atmos. Chem. Phys.*, 16, 3227-
780 3244, <http://doi.org/10.5194/acp-16-3227-2016>, 2016.

781 Heald, C. L., Jacob, D. J., Jones, D. B. A., Palmer, P. I., Logan, J. A., Streets, D. G., Sachse, G. W., Gille, J. C., Hoffman, R.
782 N., and Nehr Korn, T.: Comparative inverse analysis of satellite (MOPITT) and aircraft (TRACE-P) observations to
783 estimate Asian sources of carbon monoxide, *J. Geophys. Res.*, 109, <http://doi.org/10.1029/2004jd005185>, 2004.

784 Helmig, D., Rossabi, S., Hueber, J., Tans, P., Montzka, S. A., Masarie, K., Thoning, K., Plass-Duelmer, C., Claude, A.,
785 Carpenter, L. J., Lewis, A. C., Punjabi, S., Reimann, S., Vollmer, M. K., Steinbrecher, R., Hannigan, J. W., Emmons, L.
786 K., Mahieu, E., Franco, B., Smale, D., and Pozzer, A.: Reversal of global atmospheric ethane and propane trends largely
787 due to US oil and natural gas production, *Nature Geosci.*, 9, 490-495, <http://doi.org/10.1038/ngeo2721>, 2016.

788 Hmiel, B., Petrenko, V. V., Dyonisius, M. N., Buizert, C., Smith, A. M., Place, P. F., Harth, C., Beaudette, R., Hua, Q., Yang,
789 B., Vimont, I., Michel, S. E., Severinghaus, J. P., Etheridge, D., Bromley, T., Schmitt, J., Fäin, X., Weiss, R. F., and
790 Dlugokencky, E.: Preindustrial 14CH₄ indicates greater anthropogenic fossil CH₄ emissions, *Nature*, 578, 409-412,
791 <http://doi.org/10.1038/s41586-020-1991-8>, 2020.

792 Holmes, C. D., Prather, M. J., Søvde, O. A., and Myhre, G.: Future methane, hydroxyl, and their uncertainties: key climate and
793 emission parameters for future predictions, *Atmos. Chem. Phys.*, 13, 285-302, <http://doi.org/10.5194/acp-13-285-2013>,
794 2013.

795 Houweling, S., Krol, M., Bergamaschi, P., Frankenberg, C., Dlugokencky, E. J., Morino, I., Notholt, J., Sherlock, V., Wunch,
796 D., Beck, V., Gerbig, C., Chen, H., Kort, E. A., Röckmann, T., and Aben, I.: A multi-year methane inversion using
797 SCIAMACHY, accounting for systematic errors using TCCON measurements, *Atmos. Chem. Phys.*, 14, 3991-4012,
798 <http://doi.org/10.5194/acp-14-3991-2014>, 2014.

799 Houweling, S., Bergamaschi, P., Chevallier, F., Heimann, M., Kaminski, T., Krol, M., Michalak, A. M., and Patra, P.: Global
800 inverse modeling of CH₄ sources and sinks: an overview of methods, *Atmos. Chem. Phys.*, 17, 235-256,

801 <http://doi.org/10.5194/acp-17-235-2017>, 2017.

802 Hu, H., Landgraf, J., Detmers, R., Borsdorff, T., Aan de Brugh, J., Aben, I., Butz, A., and Hasekamp, O.: Toward Global
803 Mapping of Methane With TROPOMI: First Results and Intersatellite Comparison to GOSAT, *Geophys. Res. Lett.*, 45,
804 3682-3689, <http://doi.org/10.1002/2018gl077259>, 2018.

805 Jacob, D. J., Turner, A. J., Maasackers, J. D., Sheng, J., Sun, K., Liu, X., Chance, K., Aben, I., McKeever, J., and Frankenberg,
806 C.: Satellite observations of atmospheric methane and their value for quantifying methane emissions, *Atmos. Chem. Phys.*,
807 16, 14371-14396, <http://doi.org/10.5194/acp-16-14371-2016>, 2016.

808 Janardanan, R., Maksyutov, S., Tsuruta, A., Wang, F., Tiwari, Y. K., Valsala, V., Ito, A., Yoshida, Y., Kaiser, J. W., Janssens-
809 Maenhout, G., Arshinov, M., Sasakawa, M., Tohjima, Y., Worthy, D. E. J., Dlugokencky, E. J., Ramonet, M., Arduini, J.,
810 Lavric, J. V., Piacentino, S., Krummel, P. B., Langenfelds, R. L., Mammarella, I., and Matsunaga, T.: Country-Scale
811 Analysis of Methane Emissions with a High-Resolution Inverse Model Using GOSAT and Surface Observations, *Remote
812 Sensing*, 12, 375, <http://doi.org/10.3390/rs12030375>, 2020.

813 Janssens-Maenhout, G., Crippa, M., Guizzardi, D., Muntean, M., Schaaf, E., Dentener, F., Bergamaschi, P., Pagliari, V., Olivier,
814 J. G. J., Peters, J. A. H. W., van Aardenne, J. A., Monni, S., Doering, U., Petrescu, A. M. R., Solazzo, E., and Oreggioni,
815 G. D.: EDGAR v4.3.2 Global Atlas of the three major greenhouse gas emissions for the period 1970–2012, *Earth System
816 Science Data*, 11, 959-1002, <http://doi.org/10.5194/essd-11-959-2019>, 2019.

817 Koo, J.-H., Walker, K. A., Jones, A., Sheese, P. E., Boone, C. D., Bernath, P. F., and Manney, G. L.: Global climatology based
818 on the ACE-FTS version 3.5 dataset: Addition of mesospheric levels and carbon-containing species in the UTLS, *J. Quant.
819 Spectrosc. Radiat. Transfer*, 186, 52-62, <http://doi.org/10.1016/j.jqsrt.2016.07.003>, 2017.

820 Kuze, A., Suto, H., Shiomi, K., Kawakami, S., Tanaka, M., Ueda, Y., Deguchi, A., Yoshida, J., Yamamoto, Y., Kataoka, F.,
821 Taylor, T. E., and Buijs, H. L.: Update on GOSAT TANSO-FTS performance, operations, and data products after more
822 than 6 years in space, *Atmospheric Measurement Techniques*, 9, 2445-2461, <http://doi.org/10.5194/amt-9-2445-2016>,
823 2016.

824 Lan, X., Tans, P., Sweeney, C., Andrews, A., Dlugokencky, E., Schwietzke, S., Kofler, J., McKain, K., Thoning, K., Crotwell,
825 M., Montzka, S., Miller, B. R., and Biraud, S. C.: Long-Term Measurements Show Little Evidence for Large Increases in
826 Total U.S. Methane Emissions Over the Past Decade, *Geophys. Res. Lett.*, 46, 4991-4999,
827 <http://doi.org/10.1029/2018gl081731>, 2019.

828 Lunt, M. F., Palmer, P. I., Feng, L., Taylor, C. M., Boesch, H., and Parker, R. J.: An increase in methane emissions from tropical
829 Africa between 2010 and 2016 inferred from satellite data, *Atmos. Chem. Phys.*, 19, 14721-14740,
830 <http://doi.org/10.5194/acp-19-14721-2019>, 2019.

831 Maasackers, J. D., Jacob, D. J., Sulprizio, M. P., Turner, A. J., Weitz, M., Wirth, T., Hight, C., DeFigueiredo, M., Desai, M.,
832 Schmeltz, R., Hockstad, L., Bloom, A. A., Bowman, K. W., Jeong, S., and Fischer, M. L.: Gridded National Inventory of
833 U.S. Methane Emissions, *Environ. Sci. Technol.*, 50, 13123-13133, <http://doi.org/10.1021/acs.est.6b02878>, 2016.

834 Maasackers, J. D., Jacob, D. J., Sulprizio, M. P., Scarpelli, T. R., Nesser, H., Sheng, J.-X., Zhang, Y., Hersher, M., Bloom, A.
835 A., Bowman, K. W., Worden, J. R., Janssens-Maenhout, G., and Parker, R. J.: Global distribution of methane emissions,
836 emission trends, and OH concentrations and trends inferred from an inversion of GOSAT satellite data for 2010–2015,
837 *Atmos. Chem. Phys.*, 19, 7859-7881, <http://doi.org/10.5194/acp-19-7859-2019>, 2019.

838 Maasackers, J. D., Jacob, D. J., Sulprizio, M. P., Scarpelli, T. R., Nesser, H., Sheng, J., Zhang, Y., Lu, X., Bloom, A. A.,
839 Bowman, K. W., Worden, J. R., and Parker, R. J.: 2010–2015 North American methane emissions, sectoral contributions,
840 and trends: a high-resolution inversion of GOSAT satellite observations of atmospheric methane, *Atmos. Chem. Phys.
841 Discuss.*, <https://doi.org/10.5194/acp-2020-915>, in review, 2020.

842 Machida T., H. Matsueda, Y. Sawa and Y. Niwa, Atmospheric trace gas data from the CONTRAIL flask air sampling over the
843 Pacific Ocean, Center for Global Environmental Research, NIES, DOI:10.17595/20190828.001., 2019

844 McNorton, J., Wilson, C., Gloor, M., Parker, R. J., Boesch, H., Feng, W., Hossaini, R., and Chipperfield, M. P.: Attribution of
845 recent increases in atmospheric methane through 3-D inverse modelling, *Atmos. Chem. Phys.*, 18, 18149-18168,

846 <http://doi.org/10.5194/acp-18-18149-2018>, 2018.

847 Miller, S. M., Wofsy, S. C., Michalak, A. M., Kort, E. A., Andrews, A. E., Biraud, S. C., Dlugokencky, E. J., Eluszkiewicz, J.,
848 Fischer, M. L., Janssens-Maenhout, G., Miller, B. R., Miller, J. B., Montzka, S. A., Nehr Korn, T., and Sweeney, C.:
849 Anthropogenic emissions of methane in the United States, *Proc. Natl. Acad. Sci. U. S. A.*, 110, 20018-20022,
850 <http://doi.org/10.1073/pnas.1314392110>, 2013.

851 Miller, S. M., Michalak, A. M., Detmers, R. G., Hasekamp, O. P., Bruhwiler, L. M. P., and Schwietzke, S.: China's coal mine
852 methane regulations have not curbed growing emissions, *Nat Commun*, 10, 303, [http://doi.org/10.1038/s41467-018-](http://doi.org/10.1038/s41467-018-07891-7)
853 [07891-7](http://doi.org/10.1038/s41467-018-07891-7), 2019.

854 Monteil, G., Houweling, S., Butz, A., Guerlet, S., Schepers, D., Hasekamp, O., Frankenberg, C., Scheepmaker, R., Aben, I.,
855 and Röckmann, T.: Comparison of CH₄ inversions based on 15 months of GOSAT and SCIAMACHY observations, *J.*
856 *Geophys. Res.*, 118, 11,807-811,823, <http://doi.org/10.1002/2013jd019760>, 2013.

857 Murguia-Flores, F., Arndt, S., Ganesan, A. L., Murray-Tortarolo, G., and Hornibrook, E. R. C.: Soil Methanotrophy Model
858 (MeMo v1.0): a process-based model to quantify global uptake of atmospheric methane by soil, *Geoscientific Model*
859 *Development*, 11, 2009-2032, <http://doi.org/10.5194/gmd-11-2009-2018>, 2018.

860 Murray, L. T., Jacob, D. J., Logan, J. A., Hudman, R. C., and Koshak, W. J.: Optimized regional and interannual variability of
861 lightning in a global chemical transport model constrained by LIS/OTD satellite data, *J. Geophys. Res.*, 117, D20307,
862 <http://doi.org/10.1029/2012jd017934>, 2012.

863 Naik, V., Voulgarakis, A., Fiore, A. M., Horowitz, L. W., Lamarque, J. F., Lin, M., Prather, M. J., Young, P. J., Bergmann, D.,
864 Cameron-Smith, P. J., Cionni, I., Collins, W. J., Dalsøren, S. B., Doherty, R., Eyring, V., Faluvegi, G., Folberth, G. A.,
865 Josse, B., Lee, Y. H., MacKenzie, I. A., Nagashima, T., van Noije, T. P. C., Plummer, D. A., Righi, M., Rumbold, S. T.,
866 Skeie, R., Shindell, D. T., Stevenson, D. S., Strode, S., Sudo, K., Szopa, S., and Zeng, G.: Preindustrial to present-day
867 changes in tropospheric hydroxyl radical and methane lifetime from the Atmospheric Chemistry and Climate Model
868 Intercomparison Project (ACCMIP), *Atmos. Chem. Phys.*, 13, 5277-5298, <http://doi.org/10.5194/acp-13-5277-2013>,
869 2013.

870

871 Parker, R. J., Webb, A., Boesch, H., Somkuti, P., Barrio Guillo, R., Di Noia, A., Kalaitzi, N., Anand, J. S., Bergamaschi, P.,
872 Chevallier, F., Palmer, P. I., Feng, L., Deutscher, N. M., Feist, D. G., Griffith, D. W. T., Hase, F., Kivi, R., Morino, I.,
873 Notholt, J., Oh, Y.-S., Ohyama, H., Petri, C., Pollard, D. F., Roehl, C., Sha, M. K., Shiomi, K., Strong, K., Sussmann, R.,
874 Té, Y., Velazco, V. A., Warneke, T., Wennberg, P. O., and Wunch, D.: A decade of GOSAT Proxy satellite CH₄ observations,
875 *Earth Syst. Sci. Data*, 12, 3383–3412, <https://doi.org/10.5194/essd-12-3383-2020>, 2020.

876 Patra, P. K., Houweling, S., Krol, M., Bousquet, P., Belikov, D., Bergmann, D., Bian, H., Cameron-Smith, P., Chipperfield, M.
877 P., Corbin, K., Fortems-Cheiney, A., Fraser, A., Gloor, E., Hess, P., Ito, A., Kawa, S. R., Law, R. M., Loh, Z., Maksyutov,
878 S., Meng, L., Palmer, P. I., Prinn, R. G., Rigby, M., Saito, R., and Wilson, C.: TransCom model simulations of CH₄ and
879 related species: linking transport, surface flux and chemical loss with CH₄ variability in the troposphere and lower
880 stratosphere, *Atmos. Chem. Phys.*, 11, 12813-12837, <http://doi.org/10.5194/acp-11-12813-2011>, 2011.

881 Patra, P. K., Krol, M. C., Montzka, S. A., Arnold, T., Atlas, E. L., Lintner, B. R., Stephens, B. B., Xiang, B., Elkins, J. W.,
882 Fraser, P. J., Ghosh, A., Hints, E. J., Hurst, D. F., Ishijima, K., Krummel, P. B., Miller, B. R., Miyazaki, K., Moore, F. L.,
883 Muhle, J., O'Doherty, S., Prinn, R. G., Steele, L. P., Takigawa, M., Wang, H. J., Weiss, R. F., Wofsy, S. C., and Young, D.:
884 Observational evidence for interhemispheric hydroxyl-radical parity, *Nature*, 513, 219-223,
885 <http://doi.org/10.1038/nature13721>, 2014.

886 Patra, P. K., Saeki, T., Dlugokencky, E. J., Ishijima, K., Umezawa, T., Ito, A., Aoki, S., Morimoto, S., Kort, E. A., Crotwell,
887 A., Ravi Kumar, K., and Nakazawa, T.: Regional Methane Emission Estimation Based on Observed Atmospheric
888 Concentrations (2002-2012), *Journal of the Meteorological Society of Japan. Ser. II*, 94, 91-113,
889 <http://doi.org/10.2151/jmsj.2016-006>, 2016.

890 Pickett-Heaps, C. A., Jacob, D. J., Wecht, K. J., Kort, E. A., Wofsy, S. C., Diskin, G. S., Worthy, D. E. J., Kaplan, J. O., Bey,

891 I., and Drevet, J.: Magnitude and seasonality of wetland methane emissions from the Hudson Bay Lowlands (Canada),
892 *Atmos. Chem. Phys.*, 11, 3773-3779, <http://doi.org/10.5194/acp-11-3773-2011>, 2011.

893 Pison, I., Bousquet, P., Chevallier, F., Szopa, S., and Hauglustaine, D.: Multi-species inversion of CH₄, CO and H₂ emissions
894 from surface measurements, *Atmos. Chem. Phys.*, 9, 5281-5297, <http://doi.org/10.5194/acp-9-5281-2009>, 2009.

895 Prather, M. J., Holmes, C. D., and Hsu, J.: Reactive greenhouse gas scenarios: Systematic exploration of uncertainties and the
896 role of atmospheric chemistry, *Geophys. Res. Lett.*, 39, n/a-n/a, <http://doi.org/10.1029/2012gl051440>, 2012.

897 Rodgers, C. D.: *Inverse Methods for Atmospheric Sounding: Theory and Practice*, 2000.

898 Saunio, M., Stavert, A. R., Poulter, B., Bousquet, P., Canadell, J. G., Jackson, R. B., Raymond, P. A., Dlugokencky, E. J.,
899 Houweling, S., Patra, P. K., Ciais, P., Arora, V. K., Bastviken, D., Bergamaschi, P., Blake, D. R., Brailsford, G., Bruhwiler,
900 L., Carlson, K. M., Carrol, M., Castaldi, S., Chandra, N., Crevoisier, C., Crill, P. M., Covey, K., Curry, C. L., Etiope, G.,
901 Frankenberg, C., Gedney, N., Hegglin, M. I., Höglund-Isaksson, L., Hugelius, G., Ishizawa, M., Ito, A., Janssens-
902 Maenhout, G., Jensen, K. M., Joos, F., Kleinen, T., Krummel, P. B., Langenfelds, R. L., Laruelle, G. G., Liu, L., Machida,
903 T., Maksyutov, S., McDonald, K. C., McNorton, J., Miller, P. A., Melton, J. R., Morino, I., Müller, J., Murguia-Flores, F.,
904 Naik, V., Niwa, Y., Noce, S., O'Doherty, S., Parker, R. J., Peng, C., Peng, S., Peters, G. P., Prigent, C., Prinn, R., Ramonet,
905 M., Regnier, P., Riley, W. J., Rosentreter, J. A., Segers, A., Simpson, I. J., Shi, H., Smith, S. J., Steele, L. P., Thornton, B.
906 F., Tian, H., Tohjima, Y., Tubiello, F. N., Tsuruta, A., Viovy, N., Voulgarakis, A., Weber, T. S., van Weele, M., van der
907 Werf, G. R., Weiss, R. F., Worthy, D., Wunch, D., Yin, Y., Yoshida, Y., Zhang, W., Zhang, Z., Zhao, Y., Zheng, B., Zhu,
908 Q., Zhu, Q., and Zhuang, Q.: The Global Methane Budget 2000–2017, *Earth System Science Data*, 12, 1561-1623,
909 <http://doi.org/10.5194/essd-12-1561-2020>, 2020.

910 Scarpelli, T. R., Jacob, D. J., Maasackers, J. D., Sulprizio, M. P., Sheng, J.-X., Rose, K., Romeo, L., Worden, J. R., and
911 Janssens-Maenhout, G.: A global gridded (0.1° x 0.1°) inventory of methane emissions from oil, gas, and coal
912 exploitation based on national reports to the United Nations Framework Convention on Climate Change, *Earth System
913 Science Data*, 12, 563-575, <http://doi.org/10.5194/essd-12-563-2020>, 2020.

914 Sheng, J.-X., Jacob, D. J., Turner, A. J., Maasackers, J. D., Sulprizio, M. P., Bloom, A. A., Andrews, A. E., and Wunch, D.:
915 High-resolution inversion of methane emissions in the Southeast US using SEAC<sup>4</sup><sup>RS</sup> aircraft
916 observations of atmospheric methane: anthropogenic and wetland sources, *Atmos. Chem. Phys.*, 18, 6483-6491,
917 <http://doi.org/10.5194/acp-18-6483-2018>, 2018.

918 Sheng, J., Song, S., Zhang, Y., Prinn, R. G., and Janssens-Maenhout, G.: Bottom-Up Estimates of Coal Mine Methane
919 Emissions in China: A Gridded Inventory, Emission Factors, and Trends, *Environmental Science & Technology Letters*,
920 6, 473-478, <http://doi.org/10.1021/acs.estlett.9b00294>, 2019.

921 Stanevich, I., Jones, D. B. A., Strong, K., Parker, R. J., Boesch, H., Wunch, D., Notholt, J., Petri, C., Warneke, T., Sussmann,
922 R., Schneider, M., Hase, F., Kivi, R., Deutscher, N. M., Velazco, V. A., Walker, K. A., and Deng, F.: Characterizing model
923 errors in chemical transport modeling of methane: impact of model resolution in versions v9-02 of GEOS-Chem and v35j
924 of its adjoint model, *Geosci. Model Dev.*, 13, 3839–3862, <https://doi.org/10.5194/gmd-13-3839-2020>, 2020.

925 Thompson, R. L., Stohl, A., Zhou, L. X., Dlugokencky, E., Fukuyama, Y., Tohjima, Y., Kim, S. Y., Lee, H., Nisbet, E. G.,
926 Fisher, R. E., Lowry, D., Weiss, R. F., Prinn, R. G., O'Doherty, S., Young, D., and White, J. W. C.: Methane emissions in
927 East Asia for 2000-2011 estimated using an atmospheric Bayesian inversion, *J. Geophys. Res.*, 120, 4352-4369,
928 <http://doi.org/10.1002/2014jd022394>, 2015.

929 Turner, A. J., Jacob, D. J., Wecht, K. J., Maasackers, J. D., Lundgren, E., Andrews, A. E., Biraud, S. C., Boesch, H., Bowman,
930 K. W., Deutscher, N. M., Dubey, M. K., Griffith, D. W. T., Hase, F., Kuze, A., Notholt, J., Ohyama, H., Parker, R., Payne,
931 V. H., Sussmann, R., Sweeney, C., Velazco, V. A., Warneke, T., Wennberg, P. O., and Wunch, D.: Estimating global and
932 North American methane emissions with high spatial resolution using GOSAT satellite data, *Atmos. Chem. Phys.*, 15,
933 7049-7069, <http://doi.org/10.5194/acp-15-7049-2015>, 2015.

934 van der Werf, G. R., Randerson, J. T., Giglio, L., van Leeuwen, T. T., Chen, Y., Rogers, B. M., Mu, M., van Marle, M. J. E.,
935 Morton, D. C., Collatz, G. J., Yokelson, R. J., and Kasibhatla, P. S.: Global fire emissions estimates during 1997–2016,

936 Earth System Science Data, 9, 697-720, <http://doi.org/10.5194/essd-9-697-2017>, 2017.

937 Wang, X., Jacob, D. J., Eastham, S. D., Sulprizio, M. P., Zhu, L., Chen, Q., Alexander, B., Sherwen, T., Evans, M. J., Lee, B.
938 H., Haskins, J. D., Lopez-Hilfiker, F. D., Thornton, J. A., Huey, G. L., and Liao, H.: The role of chlorine in global
939 tropospheric chemistry, *Atmos. Chem. Phys.*, 19, 3981-4003, <http://doi.org/10.5194/acp-19-3981-2019>, 2019.

940 Waymark, C., Walker, K., Boone, C. D., and Bernath, P. F.: ACE-FTS version 3.0 data set: validation and data processing
941 update., *ANNALS OF GEOPHYSICS*, 56, <http://doi.org/10.4401/ag-6339>, 2013.

942 Wecht, K. J., Jacob, D. J., Frankenberg, C., Jiang, Z., and Blake, D. R.: Mapping of North American methane emissions with
943 high spatial resolution by inversion of SCIAMACHY satellite data, *J. Geophys. Res.*, 119, 7741-7756,
944 <http://doi.org/10.1002/2014jd021551>, 2014.

945 Zhang, B., Tian, H., Ren, W., Tao, B., Lu, C., Yang, J., Banger, K., and Pan, S.: Methane emissions from global rice fields:
946 Magnitude, spatiotemporal patterns, and environmental controls, *Global Biogeochem. Cycles*, 30, 1246-1263,
947 <http://doi.org/10.1002/2016gb005381>, 2016.

948 Zhang, Y., Jacob, D. J., Maasackers, J. D., Sulprizio, M. P., Sheng, J.-X., Gautam, R., and Worden, J.: Monitoring global
949 tropospheric OH concentrations using satellite observations of atmospheric methane, *Atmos. Chem. Phys.*, 18, 15959-
950 15973, <http://doi.org/10.5194/acp-18-15959-2018>, 2018.

951 Zhang, Y., Jacob, D. J., Lu, X., Maasackers, J. D., Scarpelli, T. R., Sheng, J.-X., Shen, L., Qu, Z., Sulprizio, M. P., Chang, J.,
952 Bloom, A. A., Ma, S., Worden, J., Parker, R. J., and Boesch, H.: Attribution of the accelerating increase in atmospheric
953 methane during 2010–2018 by inverse analysis of GOSAT observations, *Atmos. Chem. Phys. Discuss.*,
954 <https://doi.org/10.5194/acp-2020-964>, in review, 2020.

955 Zhang, Y., Gautam, R., Pandey, S., Omara, M., Maasackers, J. D., Sadavarte, P., Lyon, D., Nesser, H., Sulprizio, M. P., Varon,
956 D. J., Zhang, R., Houweling, S., Zavala-Araiza, D., Alvarez, R. A., Lorente, A., Hamburg, S. P., Aben, I., and Jacob, D.
957 J.: Quantifying methane emissions from the largest oil-producing basin in the United States from space, *Science Advances*,
958 6, eaaz5120, <http://doi.org/10.1126/sciadv.aaz5120>, 2020.

959 Zhao, Y., Saunio, M., Bousquet, P., Lin, X., Berchet, A., Hegglin, M. I., Canadell, J. G., Jackson, R. B., Hauglustaine, D. A.,
960 Szopa, S., Stavert, A. R., Abraham, N. L., Archibald, A. T., Bekki, S., Deushi, M., Jöckel, P., Josse, B., Kinnison, D.,
961 Kirner, O., Maréchal, V., amp, apos, Connor, F. M., Plummer, D. A., Revell, L. E., Rozanov, E., Stenke, A., Strode, S.,
962 Tilmes, S., Dlugokencky, E. J., and Zheng, B.: Inter-model comparison of global hydroxyl radical (OH) distributions and
963 their impact on atmospheric methane over the 2000Ó2016 period, *Atmos. Chem. Phys.*, 19, 13701-13723,
964 <http://doi.org/10.5194/acp-19-13701-2019>, 2019.

965 Zona, D., Gioli, B., Commane, R., Lindaas, J., Wofsy, S. C., Miller, C. E., Dinardo, S. J., Dengel, S., Sweeney, C., Karion, A.,
966 Chang, R. Y., Henderson, J. M., Murphy, P. C., Goodrich, J. P., Moreaux, V., Liljedahl, A., Watts, J. D., Kimball, J. S.,
967 Lipson, D. A., and Oechel, W. C.: Cold season emissions dominate the Arctic tundra methane budget, *Proc. Natl. Acad.*
968 *Sci. U. S. A.*, 113, 40-45, <http://doi.org/10.1073/pnas.1516017113>, 2016.

969

970 **Table 1.** Global sources and sinks of atmospheric methane, 2010-2017^a.

	Prior ^b	Posterior ^c
Total sources [Tg a⁻¹]	533	551
Natural Sources		
Wetlands	161	148
Open fires	14	16
Termites	12	14
Seeps	2	2
Anthropogenic sources		
Livestock	117	136
Oil	42	40
Natural gas	25	30
Coal mining	31	23
Rice cultivation	38	44
Wastewater	37	42
Landfills	30	31
Other Anthropogenic	25	25
Total Sinks [Tg a⁻¹]		
Tropospheric OH	468	456
Stratospheric loss ^d	33	33
Soil uptake ^d	34	34
Tropospheric Cl ^d	5	5

971 ^a 8-year mean values for 2010-2017.

972 ^b Prior natural source estimates (2000-2017 means) are from Bloom et al. (2017) for wetlands, Etiope et al. (2019) and
 973 Hmiel et al. (2020) for seeps, Fung et al. (1991) for termite emissions, van der Werf et al. (2017) for open fire emissions.
 974 Prior anthropogenic source estimates for 2012 are from EDGAR v4.3.2 (Janssens-Maenhout et al., 2017) except from
 975 Scarpelli et al. (2020) for fuel exploitation (oil, gas, coal), and are overwritten for the US with the gridded EPA inventory
 976 of Maasakkers et al. (2016). The prior tropospheric OH concentration field is from Wecht et al. (2014) and yields a
 977 methane lifetime against oxidation by tropospheric OH of 10.6 years.

978 ^c From the joint inversion of GOSAT and in situ data

979 ^d These minor sinks are not optimized by the inversion.

980

981 **Table 2.** Anthropogenic methane emissions and trends, 2010-2017 ^a

Inversions	In-situ-only inversion	GOSAT-only inversion	GOSAT+in situ inversion
US ^b (prior: 28 Tg a ⁻¹)			
Posterior (Tg a ⁻¹)	35	31	36
2010-2017 trend (Tg a ⁻¹ a ⁻¹)	0.5	-0.1	0.4
Canada (prior: 5 Tg a ⁻¹)			
Posterior (Tg a ⁻¹)	8	5	8
2010-2017 trend (Tg a ⁻¹ a ⁻¹)	-0.2	-0.0	-0.2
Europe ^c (prior: 27 Tg a ⁻¹)			
Posterior (Tg a ⁻¹)	28	17	23
2010-2017 trend (Tg a ⁻¹ a ⁻¹)	0.1	-0.6	-0.4
China (prior: 63 Tg a ⁻¹)			
Posterior (Tg a ⁻¹)	45	46	43
2010-2017 trend (Tg a ⁻¹ a ⁻¹)	0.3	0.4	0.1

982 ^a Posterior estimates of mean 2010-2017 emissions and trends for the in-situ-only, GOSAT-only, and GOSAT + in situ
 983 joint inversions.

984 ^b Including contiguous US and Alaska.

985 ^c Europe is defined as west of 30°E, excluding Russia.

986

987

988

989 **Table 3.** Optimized global methane budget, 2010-2017.

990

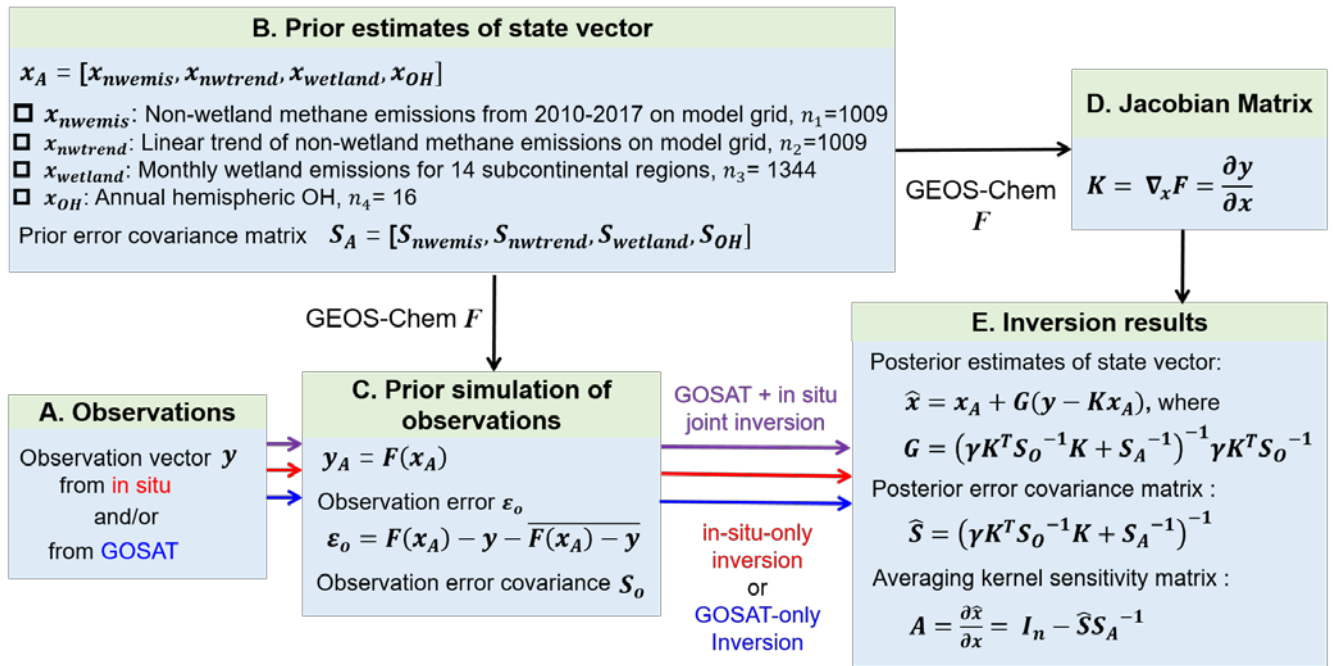
Inversions	In-situ-only inversion	GOSAT-only inversion	GOSAT+in situ inversion
Total sources [Tg a⁻¹]	515	504	551
Anthropogenic ^a	359	333	371
Seeps, termites	15	15	16
Open fires	15	16	16
Wetlands	126	140	148
Total sinks [Tg a⁻¹]	496	480	529
Tropospheric OH ^b	423	408	456
Other losses ^c	73	72	73
Mean imbalance [Tg a⁻¹]	19	24	22

991 ^a See Table 1 for sectoral breakdown from the joint inversion.

992 ^b Methane lifetime against oxidation by tropospheric OH is 11.2±0.1 years in the GOSAT + in situ inversion.

993 ^c Soils, stratosphere, and oxidation by tropospheric Cl.

994



995
 996
 997
 998
 999
 1000

Figure 1. Analytical inversion framework. The inversion is applied to GOSAT and GLOBALVIEWplus in situ observations for 2010-2017. GEOS-Chem is the chemical transport model (CTM) used as forward model for the inversion. γ is a regularization factor in the Bayesian cost function (see text).

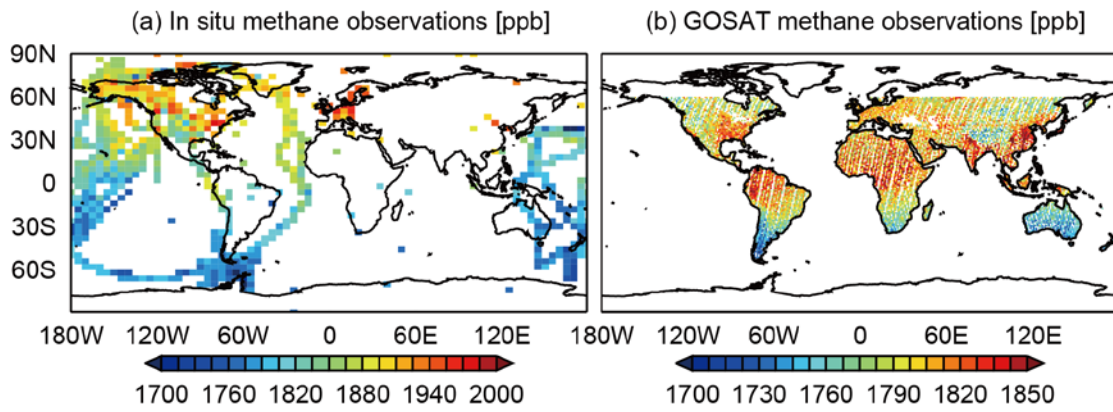


Figure.2 Mean 2010-2017 methane observations from the GLOBALVIEWplus ObsPack data product and from GOSAT. The GLOBALVIEWplus in situ data are local dry mixing ratios and are averaged over the $4^{\circ} \times 5^{\circ}$ model grid for visibility. The GOSAT data are dry column mixing ratios on a $1^{\circ} \times 1^{\circ}$ grid from the University of Leicester version 9 Proxy XCH₄ retrieval (Parker et al., 2020), excluding observations over oceans and poleward of 60° N. Note the difference in color scale between panels.

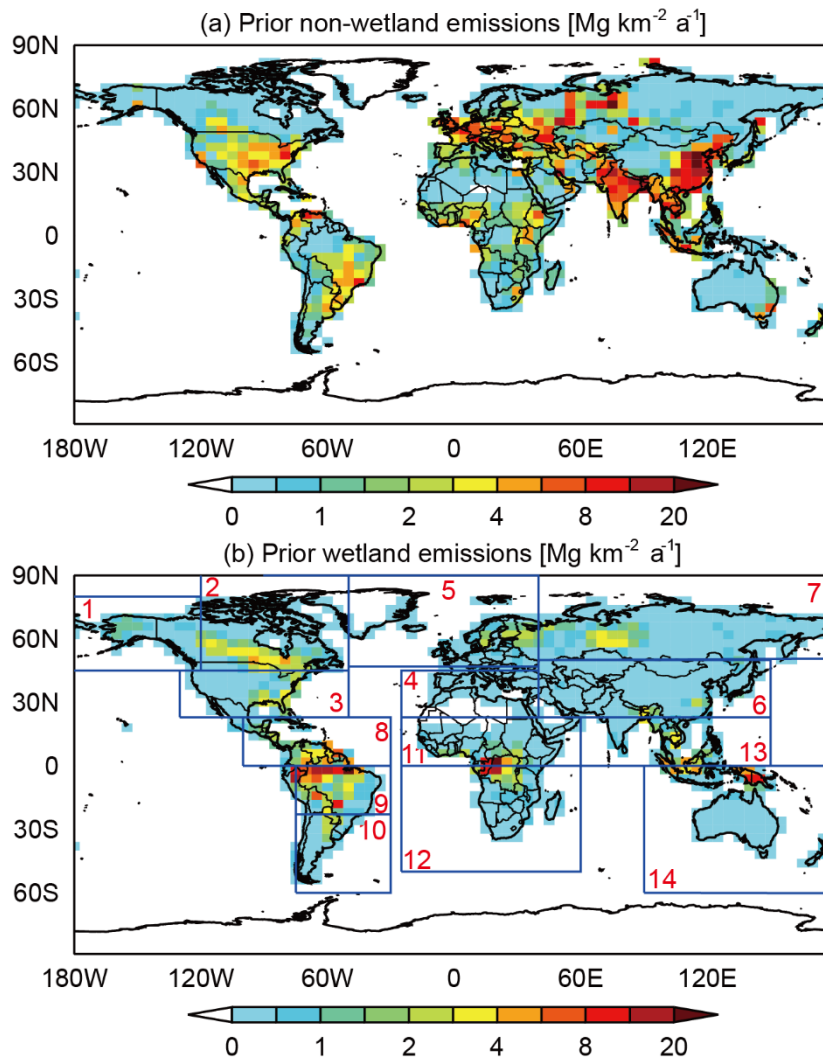


Figure 3. Prior estimates of mean 2010-2017 methane emissions. The top panel shows the non-wetland emissions on the $4^\circ \times 5^\circ$ grid used for the inversion. The bottom panel shows the wetland emissions and the 14 subcontinental wetland regions used for the inversion following Bloom et al. (2017).

Optimization of regularization parameter gamma

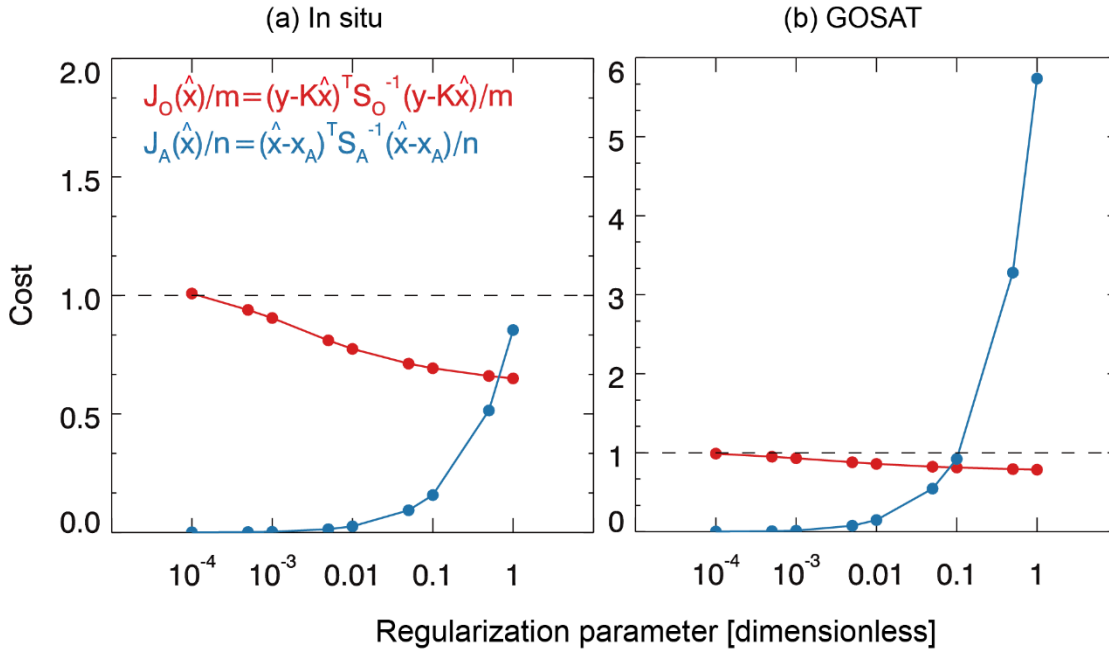
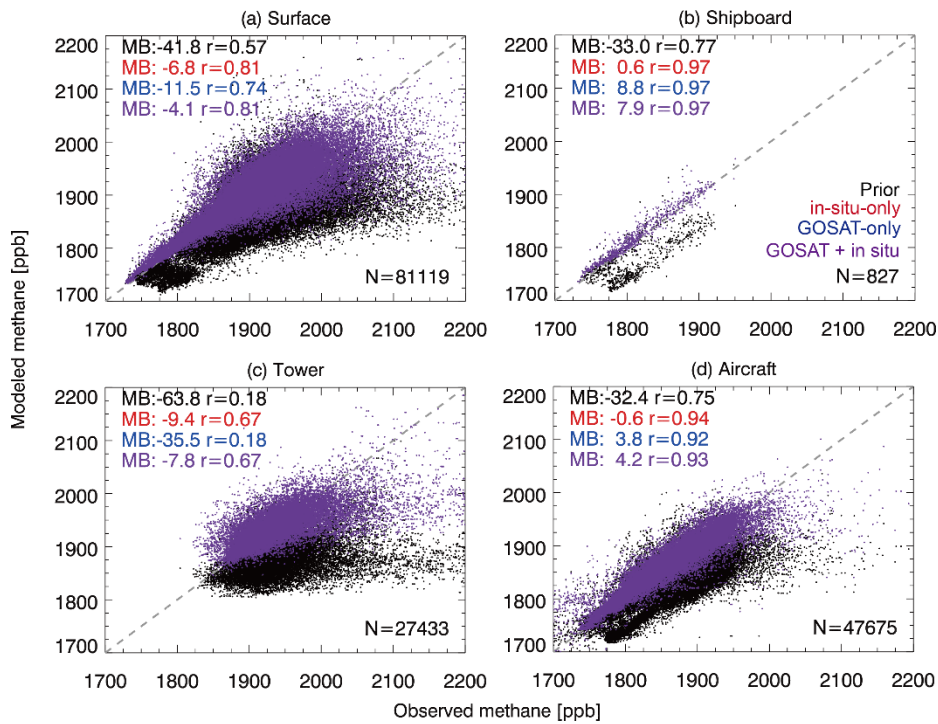


Figure 4. Optimization of the regularization parameter γ in the Bayesian cost function (Equation (1)). The figure shows the posterior observation component $J_O(\hat{\mathbf{x}}) = (\mathbf{y} - \mathbf{K}\hat{\mathbf{x}})^T \mathbf{S}_O^{-1} (\mathbf{y} - \mathbf{K}\hat{\mathbf{x}})$ and the posterior state component $J_A(\hat{\mathbf{x}}) = (\hat{\mathbf{x}} - \mathbf{x}_A)^T \mathbf{S}_A^{-1} (\hat{\mathbf{x}} - \mathbf{x}_A)$ for the insitu-only and GOSAT-only inversions.



1023

1024

1025

1026

1027

1028

1029

1030

1031

1032

Figure 5. Ability of the inversions to fit the in situ methane observations. Panels (a)-(d) compare the surface, tower, shipboard, and aircraft observations in 2010-2017 to the GEOS-Chem simulation using the prior (black) and posterior estimates of methane emissions and OH concentrations from the in-situ-only inversion (red, dots not shown), GOSAT-only inversion (blue dots not shown), and GOSAT + in situ joint inversion (purple). The numbers (N) of observations from each platform, the mean bias (MB), and the correlation coefficients (r) between the observed and simulated values are shown inset.

1033

1034

1035

Figure 6. Ability of the inversions to fit the in situ methane observations and GOSAT satellite observations. Panels (a)-(d) show the monthly time series of the differences between observed and simulated in situ methane concentrations averaged over different latitude bands from 2010 to 2017. Panels (e)-(h) are the same as panels (a)-(d) but for GOSAT methane concentrations.

1036

1037

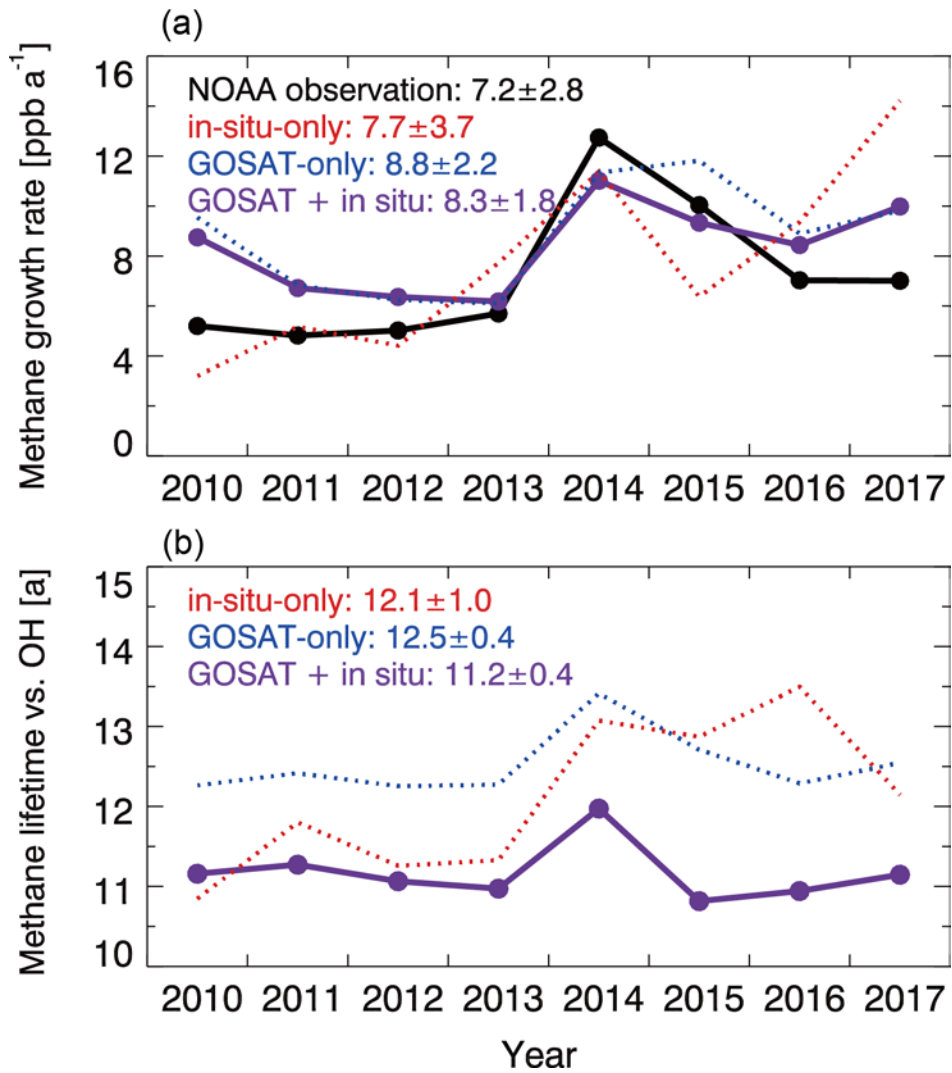
1038

1039

1040

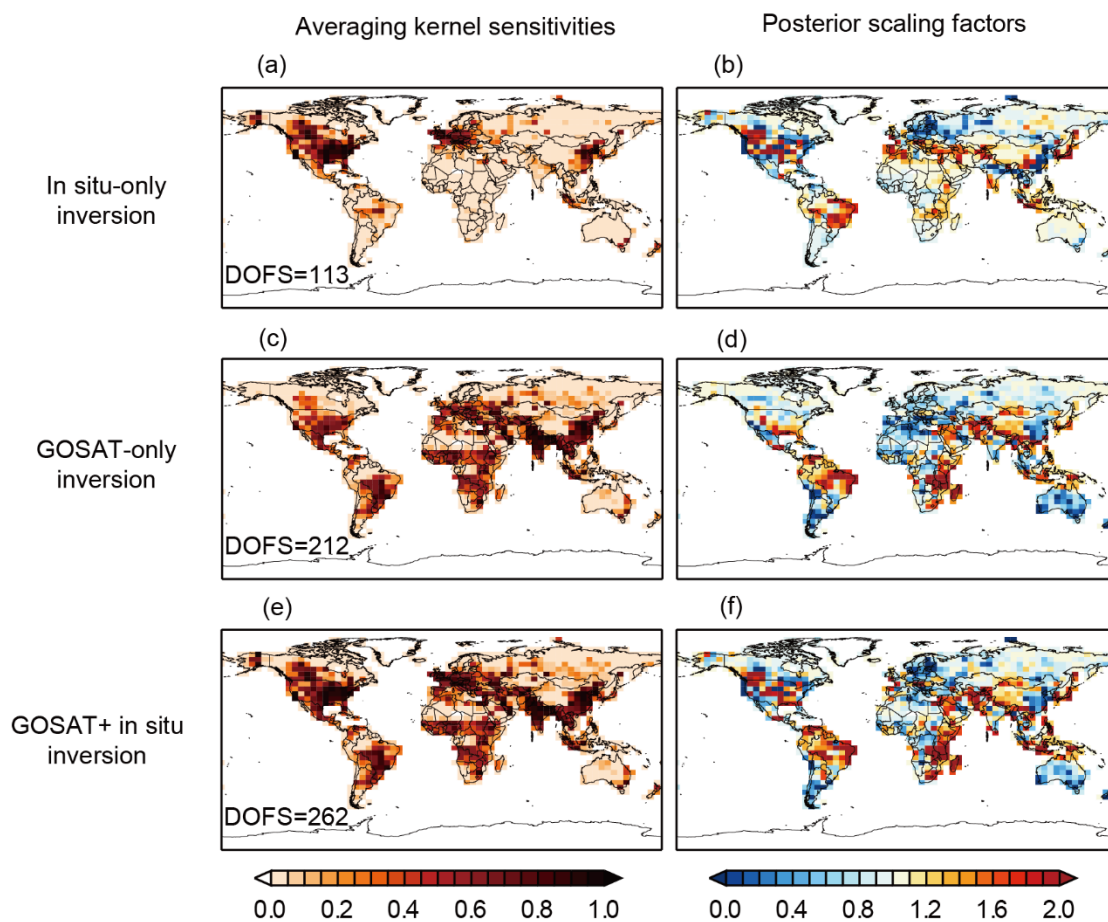
1041

34



1043
1044
1045
1046
1047
1048
1049
1050
1051

Figure 7. (a) Annual global growth rate of atmospheric methane, 2010-2017. Results from our three different inversions (in-situ-only, GOSAT-only, GOSAT + in situ) are compared to the observed growth rates inferred from the NOAA surface observational network (https://www.esrl.noaa.gov/gmd/ccgg/trends_ch4/, last access: 20 June, 2020). Mean annual growth rates and standard deviations from the different inversions are shown inset. (b). Methane lifetime against oxidation by tropospheric OH, 2010-2017, from the three different inversions. Mean lifetime and standard deviations are shown inset. The methane lifetime in the prior estimate is 10.6 years.



1052

1053

1054

1055

1056

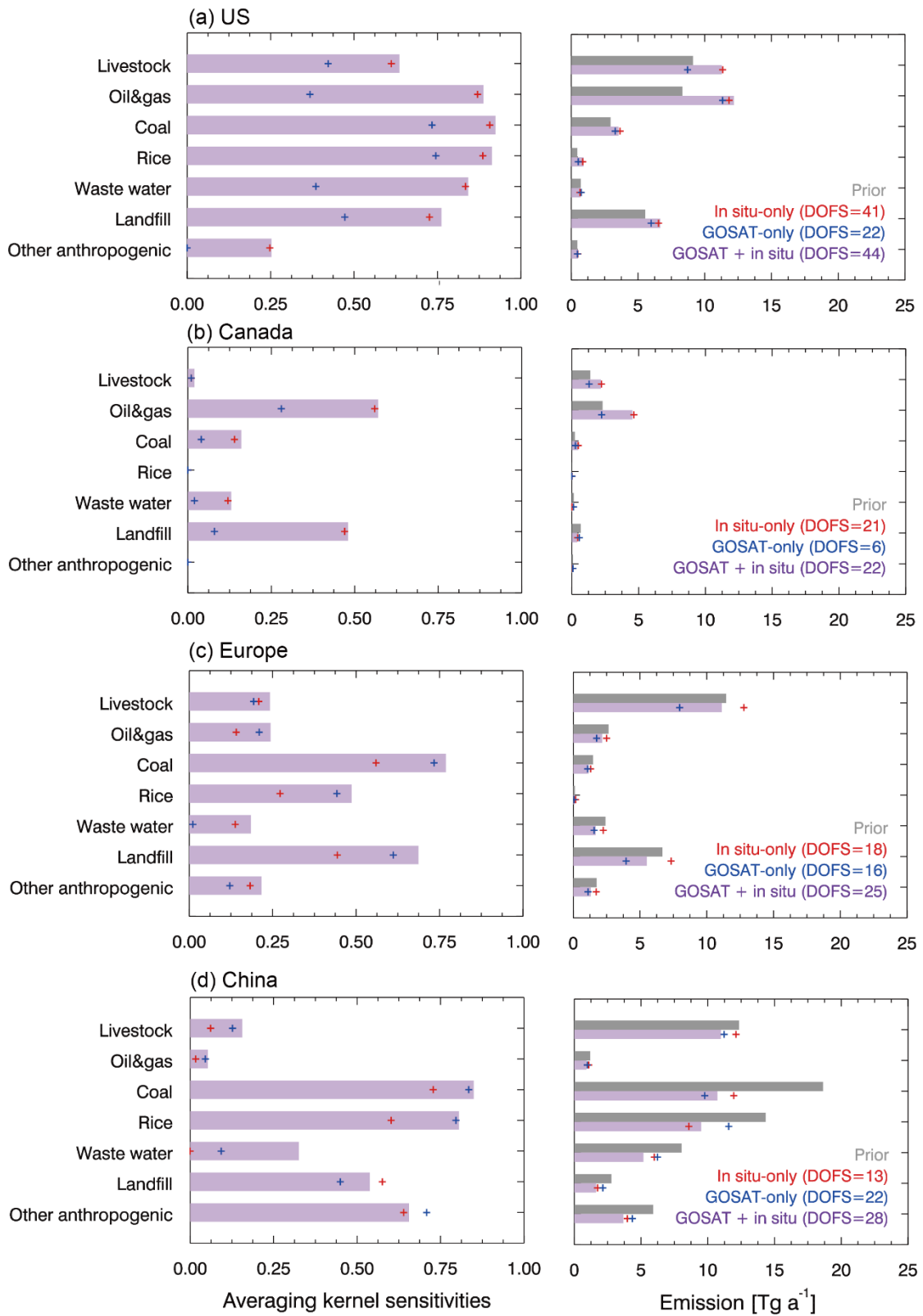
1057

1058

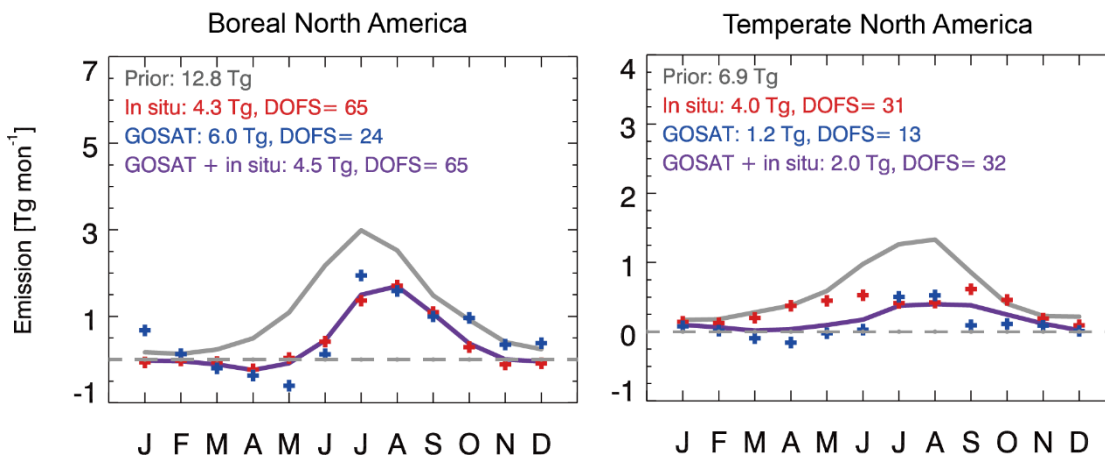
1059

1060

Figure 8. Optimization of mean 2010-2017 non-wetland (mainly anthropogenic) emissions. The in-situ-only inversion uses in situ observations, the GOSAT-only inversion uses GOSAT satellite observations, and the GOSAT + in situ inversion uses both. The left panels show the averaging kernel sensitivities (diagonal elements of the averaging kernel matrix) for each inversion, with the degrees of freedom for signal (DOFS, defined as the trace of the averaging kernel matrix) given inset. The right panels show the correction factors to the prior emissions (Figure 3a). Wetland emissions are corrected separately (see text).

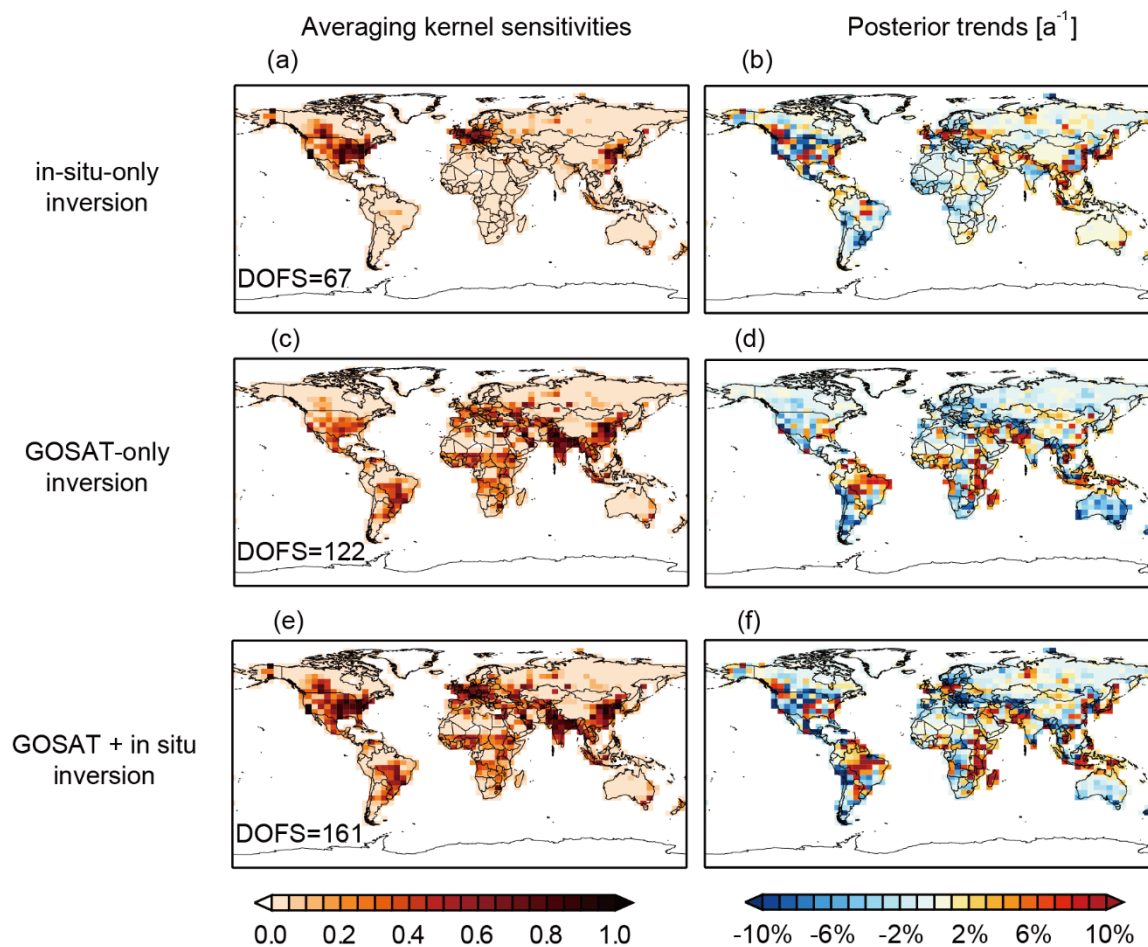


1061
 1062 **Figure 9.** Optimization of anthropogenic methane emissions by source sectors in the in-situ-only,
 1063 GOSAT-only, and GOSAT + in situ inversions. The left panel shows the averaging kernel sensitivities for
 1064 each emission sector (see text for description), the right panel shows the emissions. Europe is defined as
 1065 west of 30°E, which excludes Russia.
 1066



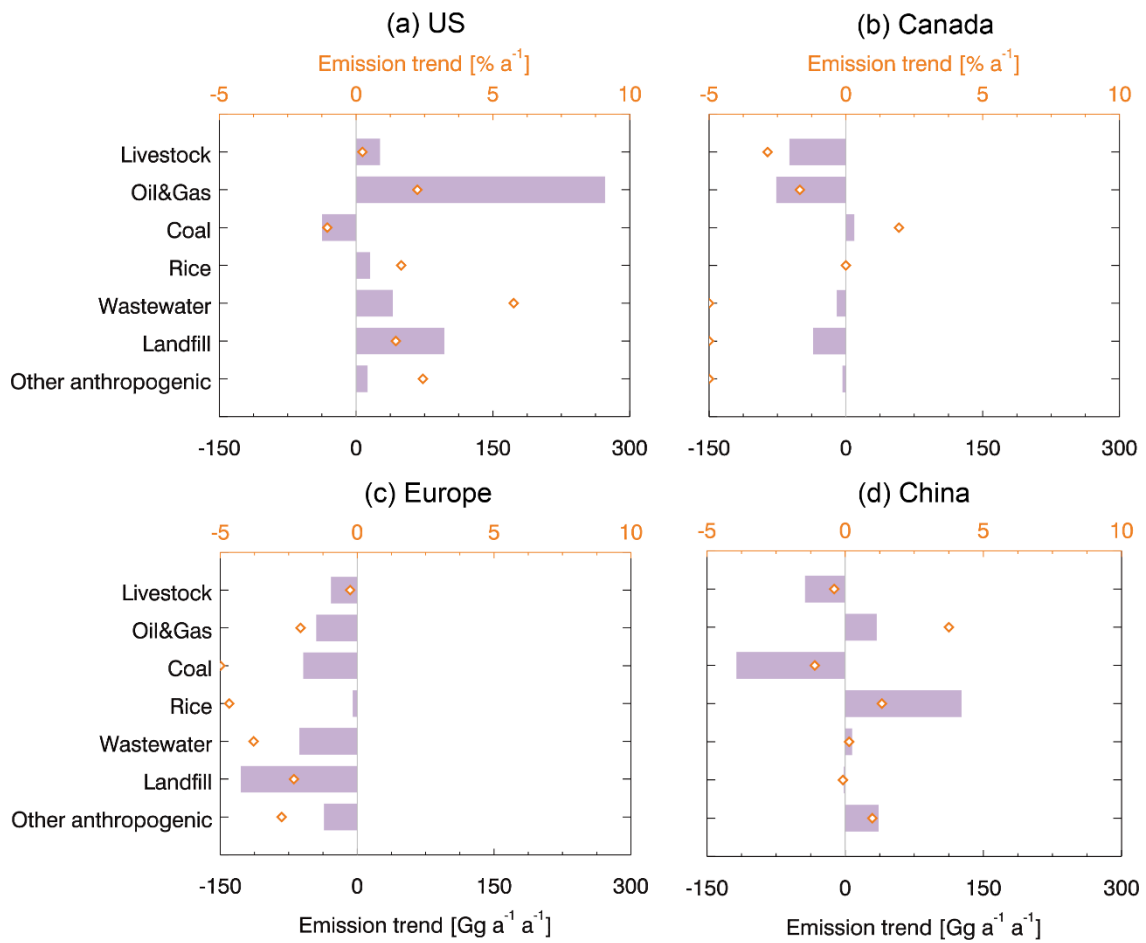
1067
 1068 **Figure 10.** Wetland emissions in boreal and temperate North America (regions 2 and 3 of Figure 3). Prior
 1069 and posterior estimates of the monthly mean wetland emissions averaged over 2010-2017 from different
 1070 inversions are shown. Annual mean emissions and the degree of freedom for signal (DOFS) for monthly
 1071 emissions in individual years are shown inset. Note differences in scale between panels. Negative
 1072 emissions are allowed statistically by the inversion but are likely not physical.
 1073

Anthropogenic methane emission trends in 2010-2017



1074
1075
1076
1077
1078

Figure 11. Same as Figure 8 but for optimization of non-wetland (mainly anthropogenic) emission trends ($\% \text{ a}^{-1}$) in 2010-2017.



1079

1080

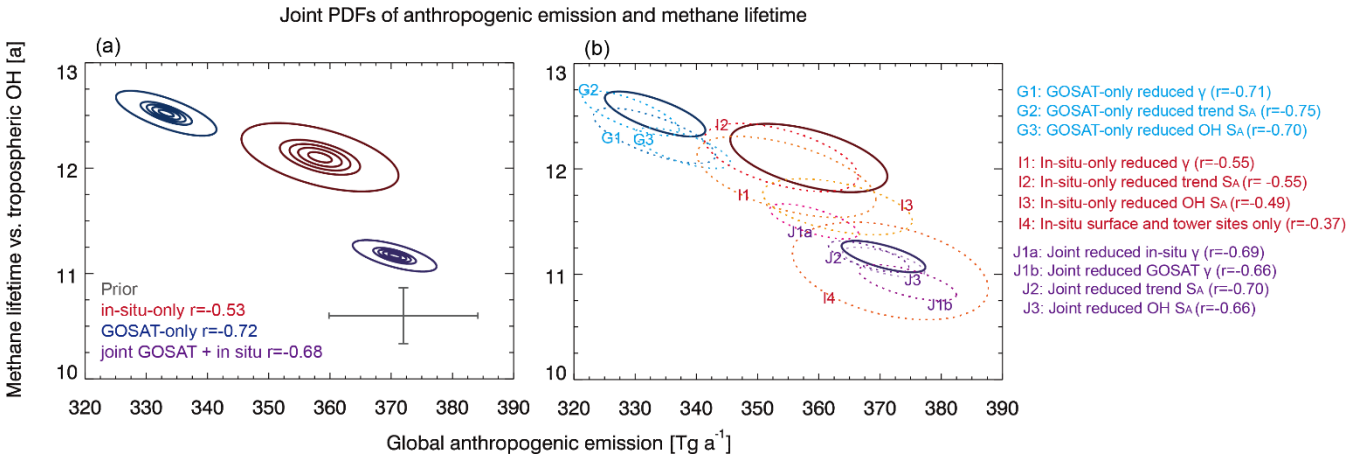
1081

1082

1083

Figure 12. Optimization by sector of regional anthropogenic methane emission trends in 2010-2017. Bars and diamonds represent trends in $\text{Gg a}^{-1} \text{a}^{-1}$ (bottom axis) and $\% \text{a}^{-1}$ (top axis) over the 2010-2017 period from the GOSAT + in situ joint inversion.

1084
1085



1086
1087
1088
1089
1090
1091
1092
1093
1094
1095
1096
1097

Figure 13. Joint probability density functions (PDFs) of global mean anthropogenic methane emission and methane lifetime against oxidation by tropospheric OH optimized by different inversions. Panel (a) shows the results from the prior and the three base inversions. The prior estimates are shown in grey with bars representing the prior error standard deviation. The thick contours show probabilities of 0.99 (outermost), 0.7, 0.5, 0.3, and 0.1 (innermost). The error correlation coefficients are given inset. Panel (b) shows the 0.99 probability contours from the three base inversions along with the same contours for ten additional sensitivity inversions using reduced values of the regularization parameter γ (0.05 instead of 0.1 for GOSAT, 0.5 instead of 1 for in situ); reduced errors for the methane emission trends on the $4^\circ \times 5^\circ$ grid (5% a^{-1} instead of 10% a^{-1}); reduced errors on annual hemispheric mean OH concentrations (5% instead of 10%); or surface and tower data only in the in-situ-only inversion.